

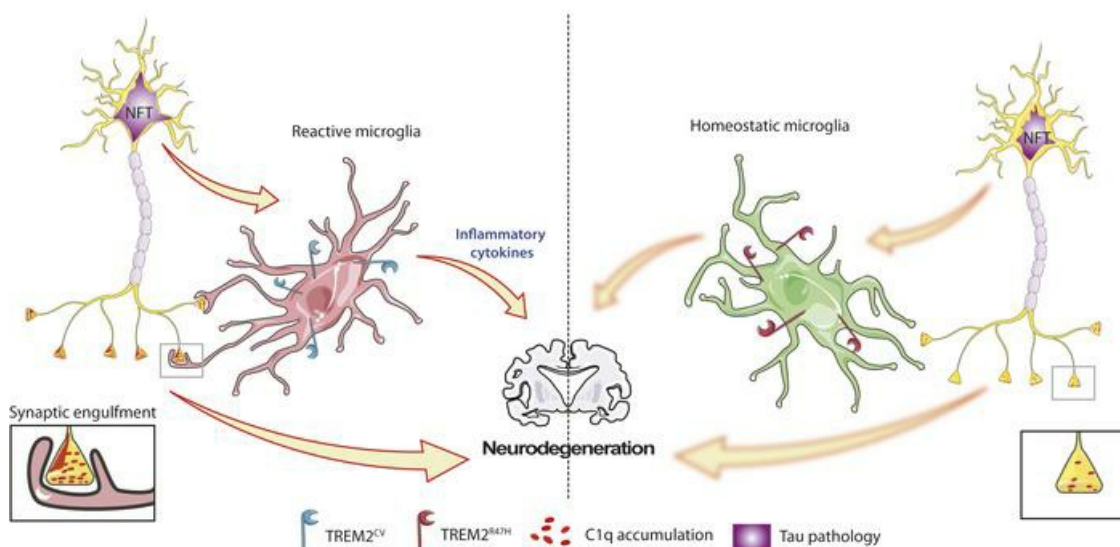
Impact of TREM2^{R47H} variant on tau pathology-induced gliosis and neurodegeneration

Maud Gratuze, ... , Jason D. Ulrich, David M. Holtzman

J Clin Invest. 2020. <https://doi.org/10.1172/JCI138179>.

Research In-Press Preview Inflammation Neuroscience

Graphical abstract



Find the latest version:

<https://jci.me/138179/pdf>



Title: Impact of TREM2^{R47H} variant on tau pathology-induced gliosis and neurodegeneration

Authors and affiliations: Maud Gratuze^{1,3,4}, Cheryl E.G. Leyns^{1,3,4}, Andrew D. Sauerbeck¹, Marie-Kim St-Pierre⁵, Monica Xiong^{1,3,4}, Nayeon Kim^{1,3,4}, Javier Remolina Serrano^{1,3,4}, Marie-Ève Tremblay⁵, Terrance T. Kummer¹, Marco Colonna^{2,3,4}, Jason D. Ulrich^{1,3,4}, and David M. Holtzman^{1,3,4*}

¹Department of Neurology, ²Department of Pathology and Immunology, ³Hope Center for Neurological Disorders, ⁴Knight Alzheimer's Disease Research Center, Washington University School of Medicine, St. Louis, MO, USA, ⁵Axe Neurosciences, CRCHU de Québec-Université Laval, Québec, QC, Canada

Corresponding Author: * For correspondence contact David M. Holtzman, Department of Neurology, Hope Center for Neurological Disorders, Charles F. and Joanne Knight Alzheimer's Disease Research Center, Washington University School of Medicine, 660 S. Euclid Avenue, Box 8111, St. Louis, Missouri, 63110, USA. Phone: +1-314-747-0644 ; Email: holtzman@wustl.edu.

Conflict of interest statement: D.M.H. and J.D.U. are listed as inventors on a provisional patent from Washington University on TREM2 antibodies. D.M.H. and C.E.G.L. are listed as inventors on a patent licensed by Washington University to C2N Diagnostics on the therapeutic use of anti-tau antibodies. C.E.G.L. is currently an employee at Merck. M.C. receives research funding from Alector, Amgen, and Ono. D.M.H. co-founded and is on the scientific advisory board of C2N Diagnostics. C2N Diagnostics has licensed certain anti-tau antibodies to AbbVie for therapeutic development. D.M.H. is on the scientific advisory board of Denali and consults for Genentech and Idorsia. All other authors have no competing interests.

Abstract:

Alzheimer's disease (AD) is characterized by amyloid- β -containing plaques and neurofibrillary tangles composed of aggregated, hyperphosphorylated tau. Beyond tau and A β , evidence suggests that microglia play an important role in AD pathogenesis. Rare variants in the microglial-expressed triggering receptor expressed on myeloid cells 2 (*TREM2*) gene increase AD risk 2-4-fold. It is likely that these TREM2 variants increase AD risk by decreasing the response of microglia to A β and its local toxicity. However, neocortical A β pathology occurs many years before neocortical tau pathology in AD. Thus, it will be important to understand the role of TREM2 in the context of tauopathy. We investigated the impact of the AD-associated TREM2 variant (R47H) on tau-mediated neuropathology in the PS19 mouse model of tauopathy. We assessed PS19 mice expressing human TREM2^{CV} (common variant) or human TREM2^{R47H}. PS19-T2^{R47H} mice had significantly attenuated brain atrophy and synapse loss vs. PS19-T2^{CV} mice. Gene expression analyses and CD68 immunostaining revealed attenuated microglial reactivity in PS19-T2^{R47H} vs. PS19-T2^{CV} mice. There was also a decrease in phagocytosis of postsynaptic elements by microglia expressing TREM2^{R47H} in the PS19 mice and in human AD brains. These findings suggest that impaired TREM2 signaling reduces microglia-mediated neurodegeneration in the setting of tauopathy.

Brief Summary: In a mouse model of tauopathy, expression of the TREM2^{R47H} variant results in decreased microgliosis, neurodegeneration, and synapse loss compared to the common variant.

Introduction:

Alzheimer's disease (AD) is the leading cause of dementia worldwide and is the 6th leading cause of death in the United States (1). The histopathological hallmarks of AD are extracellular amyloid plaques composed predominantly of the amyloid- β (A β) peptide and neurofibrillary tangles (NFTs) within neurons consisting of abnormally aggregated, hyperphosphorylated tau protein (for reviews (2–4)). Beyond tau and A β pathologies, neuroinflammatory changes are present in AD and in primary tauopathies (5), including alterations in the morphology, reactivity, distribution and gene expression of microglia. The gene expression changes that occur in microglia in the presence of amyloid, tau, and other pathologies have been termed by some as disease-associated microglia (DAM) (6) or the microglial neurodegenerative phenotype (MGnD) (7). In the DAM and MGnD phenotypes, there is a downregulation of so-called homeostatic microglial genes such as *P2ry12*, *Tmem119* and *Cx3cr1*, while there is an increase in the expression of several other genes such as *ApoE*, *Tyrobp* and *Trem2* (6, 7). However, the exact contributions of innate immune activation to different types of pathologies and neurodegeneration are still not clear.

In the last decade, several novel genetic factors linked with increased risk of AD have been identified thanks to new whole-genome sequencing and genome wide association studies (GWAS). Interestingly, many of these genetic risk factors encode proteins involved in microglial function and inflammation including TREM2, CD33, CR1, ABCA7, SPI1 and SHIP1 (8). Particular interest has been given to the microglial-expressed triggering receptor expressed on myeloid cells 2 (TREM2), since rare variants in the *TREM2* gene increase AD risk 2-4-fold (9, 10). TREM2 is a receptor that belongs to the immunoglobulin superfamily and is expressed on myeloid cells such as microglia in the brain (11, 12). TREM2 signaling is associated with a number of downstream cellular processes including proliferation and survival, suppression of toll-like receptor-induced inflammatory cytokine production, and facilitation of metabolic ATP production (13). Several TREM2 variants have been shown to impair but not block functional TREM2 signaling resulting in the partial loss-of-function of the receptor. The most common AD-associated TREM2 variant is rs75932628, a single nucleotide polymorphism encoding an arginine-

to-histidine missense substitution at amino acid 47 (R47H) (9, 10). The TREM2^{R47H} variant results in decreased TREM2 signaling upon ligand-induced stimulation (14, 15).

In order to better understand the role of TREM2 and AD-associated *TREM2* variants in AD pathogenesis, several studies have used models of AD pathology. *In vivo* studies in mouse models of amyloid deposition indicate a critical function for TREM2 in the clustering of microglia around plaques, plaque compaction, microglial proliferation and phagocytosis, and in decreasing A β -induced neuritic dystrophy and tau seeding/spreading. TREM2 knockout or expression of the TREM2^{R47H} variant have been shown to affect these phenotypes in the opposite direction (14–18). These studies suggest that TREM2 signaling is protective in decreasing A β -mediated local injury and in exacerbating the A β -induced spreading of tau pathology. However, in AD and in primary tauopathies, the accumulation of aggregated, hyperphosphorylated tau, and not A β , strongly correlates with local brain atrophy and neuronal death. In AD, the accumulation of pathological forms of tau in the neocortex associated with atrophy and cell death doesn't begin to occur until about 15-25 years after the onset of A β deposition (19). The role of TREM2 and *TREM2* variants linked to AD in the setting of tauopathy has been much less studied. However, numerous clues in the literature suggest a link between tau pathology and TREM2 in AD. In the cerebrospinal fluid (CSF) of AD patients, soluble TREM2 has been shown to correlate with total and phosphorylated tau (Thr181) levels (20, 21). Moreover, AD patients harboring the R47H variant of TREM2 display higher levels of both total tau and phosphorylated tau (Thr181) in CSF compared to non-carriers (22, 23). Importantly, levels of phosphorylated tau in the CSF correlate with tau pathology burden in the brain and with neuronal loss and cognitive decline in AD patients (24). Previously, we reported a decrease in brain atrophy as well as attenuated microgliosis in the brains of PS19 mice lacking TREM2 without a significant change in tau pathology (25). In another study, Sayed et al. also found that TREM2 knockout protected against tau-mediated microglial reactivity and atrophy (25), but that TREM2 haplo-insufficiency was associated with elevated expression of proinflammatory markers, exacerbated atrophy and increased tau pathology in PS19 mice (26). Finally, Bemiller et al. crossed TREM2 knockout mice with hTau mice, a less aggressive mouse model of tauopathy, and identified a decrease in microgliosis in TREM2-deficient hTau mice (27), as observed in TREM2-deficient PS19 mice, but

reported that complete deletion of TREM2 in hTau mice exacerbated tau pathology related markers. These studies in primary tauopathy mouse models suggest that TREM2 may play a dual role depending on the disease stages: during early stages of tau pathology development in the absence of neurodegeneration (e.g. hTau mice), decreased TREM2 function might promote tau pathology, while the complete loss of TREM2 function in advanced stages (PS19 mice) of the disease seems to protect from neurodegeneration. However, no study has evaluated the impact of AD-associated TREM2 variants, such as R47H variant, in the setting of a model of pure tauopathy, nor in a model that develops robust neurodegeneration as is seen in tau-related neurodegenerative diseases.

Given the emerging role for microglia in tau-mediated neuropathology, it is important to understand the role of AD-associated *TREM2* variants which decrease, but do not eliminate, TREM2 signaling in the context of tauopathy and its associated neurodegeneration. Therefore, we investigated the impact of the most prominent AD-associated *TREM2* variant (R47H) on tau pathology and tau-mediated brain damage in the PS19 mouse model of tauopathy. PS19 mice were crossed with mice expressing human *TREM2*^{CV} (common variant) or human *TREM2*^{R47H} lacking the endogenous murine *Trem2* gene. We hypothesized that *TREM2*^{R47H} would result in decreased microglial inflammatory response and would protect against tau-dependent neurodegeneration. We observed that PS19-T2^{R47H} mice have reduced phospho-tau staining compared to PS19-T2^{CV} mice. Moreover, PS19-T2^{R47H} mice have significantly attenuated brain atrophy and synapse loss compared to PS19-T2^{CV} mice. Gene expression analyses and CD68 immunostaining revealed attenuated microglial reactivity in PS19-T2^{R47H} vs. PS19-T2^{CV} mice. Importantly, a decrease in phagocytosis of postsynaptic elements by microglia expressing *TREM2*^{R47H} was detected in PS19 mice and in post-mortem human AD brains. Collectively, these findings suggest that reduced TREM2 signaling reduces microglial conversion to a more pro-inflammatory, phagocytic state and is protective against neurodegeneration in the setting of advanced tauopathy.

Results:

Effects of TREM2^{R47H} on pTau pathology. To determine whether the presence of the R47H variant of TREM2 affects tau pathology and tau-related inflammation and neurodegeneration, we utilized the PS19 tauopathy mouse model that overexpresses 1N4R human tau containing the P301S mutation that causes a familial form of frontal temporal dementia (FTD). By 9 months of age, this model develops strong tau hyperphosphorylation and aggregation, neurofibrillary tangle deposition, and gliosis, as well as neuronal loss, brain atrophy and loss of synaptic proteins in specific brain regions including the hippocampus, entorhinal cortex, piriform cortex, and amygdala (28, 29). We crossed PS19 mice on a mouse TREM2 KO background with bacterial artificial chromosome (BAC) transgenic mouse lines expressing either the human common variant of TREM2 (TREM2^{CV}) or the AD-associated human R47H variant of TREM2 (TREM2^{R47H}) on a mouse TREM2 KO background (15). Importantly, TREM2^{CV} and TREM2^{R47H} mice express a similar level of TREM2 protein in the brain and expression of TREM2^{CV}, but not TREM2^{R47H}, rescues TREM2-dependent phenotypes such as plaque-associated microgliosis (15).

At 3 months of age, prior to the overt onset of tau pathology, we observed reduced phosphorylated tau staining on serine 202-threonine 205, in the hippocampus (Fig. S1 B and D) and piriform cortex (Fig. S1 A and C) of PS19-T2^{R47H} mice compared to PS19-T2^{CV} mice, although the change was only statistically significant in the hippocampus. Staining with AT180 (p.Thr231) and PG5 (p.Ser409) did not reveal any significant differences in phosphorylated tau between PS19-T2^{R47H} mice and PS19-T2^{CV} mice in the piriform cortex (Fig. S1 E, G and I, K) or hippocampus (Fig. S1 F, H and J, L). To further examine tau and pTau levels in these mice, we performed a biochemical extraction of hippocampal brain tissue and measured the concentration of pTau and total tau using a pTau-specific (p.Ser202-Thr202 and p.Thr181) and htau-specific ELISA. We observed no significant differences in pTau (Fig. S1 M) and tau levels (Fig. S1 N) as well as in the pTau/tau ratio (Fig. S1 O) between PS19-T2^{R47H} mice and PS19-T2^{CV} mice. At 9 months of age, when substantial tau pathology had developed, we again observed a significant decrease in hippocampal phosphorylated tau staining on serine 202-threonine 205 (Fig. 1 B and D) as well as on serine 409 (Fig. 1 J and L) between PS19-T2^{R47H} and PS19-T2^{CV} mice. There was no significant difference observed on these pTau epitopes in the piriform cortex (Fig. 1 A, C and I, K).

Interestingly, staining pTau on threonine 231 revealed less phosphorylated tau in the piriform cortex of PS19-T2^{R47H} mice compared to PS19-T2^{CV} mice (Fig. 1 F and H), but no difference in the hippocampus (Fig. 1 E and G). Biochemical analysis of pTau in hippocampal brain tissue samples by ELISA revealed no significant differences in pTau level (Fig. 1 M) but increased total tau levels in PS19-T2^{R47H} mice compared to PS19-T2^{CV} mice (Fig. 1 N), resulting in a slight but not statistically significant ($p=0.0815$) decrease in pTau/tau ratio (Fig. 1 O) in PS19-T2^{R47H} mice compared to PS19-T2^{CV} mice. These findings demonstrate that the R47H variant of TREM2 significantly attenuates increases in pTau on some tau sites mostly in the later stages of tau pathology in PS19 mice. Interestingly, we (25) and others (27) did not observe lower pTau pathology in PS19 mice deleted for TREM2 compared to PS19 mice. New studies will be needed to better understand this difference, but we can hypothesize that the human TREM2^{CV} assessed in the present study has a slightly different impact on tau pathology than mouse TREM2 used in the previous studies.

Effects of TREM2^{R47H} on brain atrophy. Because pathological tau is directly linked to neurodegeneration, we next evaluated the brain volume of these mice. As expected, no change in brain volume was detected between PS19-T2^{R47H} and PS19-T2^{CV} mice at 3-months of age which is prior to when neurodegeneration has been observed in this model (Fig. S2 A-E). At 9 months of age when tau pathology is much more substantial and neurodegeneration is usually marked in specific brain regions in this model, the presence of the R47H variant of TREM2 strongly attenuated brain atrophy in PS19 mice compared to mice expressing the TREM2^{CV} (Fig. 2 A and E) similar to PS19 mice lacking for TREM2 (25). More specifically, atrophy was significantly decreased by ~ 24% in the hippocampus (Fig. 2 B) and by ~ 34% in the piriform/entorhinal cortex (Fig. 2 D). When atrophy occurs in hippocampal and cortical regions, there is concomitant enlargement of the lateral ventricles. TREM2^{R47H} was also associated with extensively reduced ventricular dilatation (~67%) in 9-month-old PS19 mice (Fig. 2 C). Then, we estimated the neuronal loss by measuring the thickness of the granule cell layer in the dentate gyrus (DG) and the pyramidal cell layer in the piriform cortex in 9-month-old mice. In accordance with changes observed in brain volume, both granule cell layer in DG (Fig. 2 G and I) and pyramidal cell layer in the piriform cortex (Fig. 2 F and H) were visibly and significantly thicker in PS19-T2^{R47H} compared to PS19-T2^{CV} mice. This strikingly reduced neurodegeneration suggests an important role for

TREM2 in regulating tau-mediated brain atrophy with the R47H variant of TREM2 being neuroprotective in the setting of tauopathy.

Effects of TREM2^{R47H} on microglial and astrocyte phenotypes. Microglia are critical mediators of tau-dependent neurodegeneration (28, 30). Given that the TREM2^{R47H} variant affects microglial function, and that PS19-T2^{R47H} mice exhibited reduced neurodegeneration, we hypothesized that we would also observe a state of reduced microglial reactivity as reflected by staining with certain microglial markers. We assessed brain sections with the myeloid immune cell marker ionized calcium binding adaptor molecule 1 (Iba1) to assess the overall microglia population. At 3 months of age, before the onset of overt tau pathology, there was no change in the surface area covered by microglia in the piriform cortex (Fig. S3 A and C) or the hippocampus (Fig. S3 B and D) between PS19-T2^{R47H} and PS19-T2^{CV} mice. When we assessed microglial coverage in 9-month-old mice, we observed a marked decrease of Iba1 staining in the piriform cortex (Fig. 3 B and D) and the hippocampus (Fig. 3 C and E) of PS19-T2^{R47H} in comparison to PS19-T2^{CV} mice. Consistent with these results, Iba1 gene expression was reduced by ~ 32% in the cortex of PS19-T2^{R47H} vs. PS19-T2^{CV} mice (Fig. 3 A). Importantly, reduced microgliosis induced by TREM2^{R47H} in PS19 mice was qualitatively similar to previous observations when TREM2 is deleted in the same mouse model (25).

We next assessed microglial phenotypic and functional changes in the mice (Fig. 4). CD68 (cluster of differentiation 68) labeling, a marker of phagolysosomal activity, was drastically reduced in the piriform cortex (Fig. 4 C) and the hippocampus (Fig. 4 D) of 9-month-old PS19-T2^{R47H} compared to PS19-T2^{CV} mice. Strikingly, there was a decrease of CD68 staining of ~ 78% per Iba1+ cell volume detected in PS19-T2^{R47H} vs. PS19-T2^{CV} brains (Fig. 4 E and F), confirming a reduced activation state of PS19-T2^{R47H} microglia. We also assessed the microglial gene expression profile in the cortex of 9-month-old PS19-T2^{R47H} and PS19-T2^{CV} (Fig. 4 G). Consistent with lower CD68 staining in PS19-T2^{R47H} mice, all the disease-associated microglia (DAM) genes tested were downregulated in PS19-T2^{R47H} compared to PS19-T2^{CV} mice such as *axl*, *cst7* and *cd9*. Interestingly, an increase in the expression of the homeostatic gene *P2ry12* was observed in PS19-T2^{R47H} mice, suggesting a more homeostatic status of microglia compared to PS19-T2^{CV} mice. On the other hand, *Cx3cr1* gene expression was decreased in PS19 mice expressing the

R47H variant of TREM2, which may be due to a lower number of microglia in these mice. Evaluation of several inflammatory cytokine genes revealed a significant decrease in pro-inflammatory mediators such as IL1 α , IL1 β , TNF α and TGF β . IL6 gene expression was not altered by the AD-associated TREM2 variant in PS19 mice, as previously reported in PS19 knock-out for TREM2 (31).

Another brain cell type, astrocytes, also plays an essential role in neuroinflammation. It has been previously shown that reactive microglia can induce astrogliosis through the production of cytokines as IL1 α and TNF α that can promote neuronal death (32, 33). As previously observed in PS19 mice lacking TREM2 (25), we found that glial fibrillary acidic protein (GFAP) gene expression, a marker of reactive astrocytes, was decreased in 9-month-old PS19-T2^{R47H} compared to PS19-T2^{CV} mice (Fig. S4 A). In addition, the GFAP signal was drastically reduced in the piriform cortex (Fig. S4 B and D) of PS19-T2^{R47H} compared to PS19-T2^{CV} mice, but not in the hippocampus (Fig. S4 E and C). Taken together, these data suggest that the R47H variant of TREM2 strongly reduced microglial activation and the concomitant astrogliosis in the setting of tauopathy.

Effects of TREM2^{R47H} on synapses. A recent study by Dejanovic et al. reported a striking accumulation of complement C1q in synapses of PS19 mice and AD patients (34). Synaptic C1q accumulation correlated with augmented microglial engulfment of synapses *in vivo* and decline of synapse density *in vitro*. Since we previously showed that C1q gene expression can be modulated by the absence of TREM2 in PS19 mice, we assessed how TREM2^{R47H} affected protein and gene expression level of C1q, as well as C1q+ synapses in PS19 mice. First, we found that C1qa gene expression was reduced by ~ 60% in the cortex of 9-month-old PS19-T2^{R47H} compared to the PS19-T2^{CV} mice (Fig. 5 C). Consistent with these findings, C1q staining and confocal analysis revealed reduced C1q staining in PS19-T2^{R47H} (Fig. 5 B). To evaluate C1q accumulation at putative synapses, we then assessed the number of puncta labeled with pre- and post-synaptic markers that were positive for C1q. PSD-95 puncta and synapsin puncta positive for C1q were significantly decreased in PS19-T2^{R47H} vs. PS19-T2^{CV} mice (Fig. 5 A, D and E).

We next assessed whether the decrease in C1q-opsonized synaptic marker puncta and attenuated brain atrophy would correspond to improved synaptic integrity in PS19-T2^{R47H} mice. We therefore quantified pre-synaptic (synapsin) and post-synaptic (PSD-95) marker puncta in

PS19-T2^{R47H} and PS19-T2^{CV} mice in the polymorphic layer of the piriform cortex (Fig. 6 A). This revealed significantly more pre- and post-synaptic puncta in PS19-T2^{R47H} compared to PS19-T2^{CV} mice (Fig. 6 B and C). As many such puncta are non-synaptic (35, 36), we turned to a more specific method of quantifying intact synaptic loci. Using SEQUIN analysis (Synaptic Evaluation and Quantification by Imaging of Nanostructure(36), a super-resolution imaging and image analysis platform for quantifying synaptic loci, we detected significantly more intact synaptic loci in PS19 mice expressing the R47H vs. the CV variant of TREM2 (Fig. 6 D). To better understand ultrastructural changes at synapses under these conditions, electron microscopy was undertaken in a small parallel cohort in the polymorphic layer of the piriform cortex. Synapses from PS19-T2^{CV} mice exhibited several dystrophic features, including swollen pre-synaptic elements, accumulation of enlarged autophagosomes, and a reduced number of synaptic vesicles (Fig. 6 E). Moreover, mitochondria often appeared swollen, a feature also seen with hypoxia, and abundant “dark” dendritic spines, indicative of post-synaptic cellular stress, were visible (Fig. 6 E). In contrast, electron microscopy images from PS19-T2^{R47H} mice revealed improved synaptic integrity with fewer autophagosomes, preserved mitochondrial ultrastructure and less frequent dark dendrites/spines and axon terminals (Fig. 6 F). Importantly, these results demonstrate that reduced brain atrophy in PS19 mice harboring TREM2^{R47H} is associated with decreased synapses with dystrophic features and better preservation pre- and post-synaptic elements.

Effects of TREM2^{R47H} on microglial phagocytosis of synaptic elements. Regarding the role of TREM2 in microglial phagocytosis (37, 38) and the fact that we observed strong reduction of CD68+ phagolysosomes in microglia of PS19-T2^{R47H} vs. PS19-T2^{CV} mice, we then hypothesized that impairment of microglial phagocytosis in 9-month-old PS19-T2^{R47H} mice is responsible for the decreased synapse loss. A previous study by Filipello et al. (39) demonstrating that microglial TREM2 is required for synapse elimination during the early stages of brain development strongly support this hypothesis. Co-staining and confocal analysis for the microglial phago-lysosomal marker CD68 and the post-synaptic marker PSD-95 revealed significantly lower PSD-95 puncta in CD68+ vesicles per microglia in the polymorphic layer of the piriform cortex of 9-month-old PS19-T2^{R47H} compared to PS19-T2^{CV} mice (Fig. 7 A and B). Consistent with the higher content of synapses in 9-month-old PS19-T2^{R47H} mice, these data show an important role for TREM2 in

synapse loss in PS19 mice that is decreased by the R47H variant of TREM2 in a pure tauopathy model.

Given these results, to assess the relevance of these findings in the setting of tauopathy in human AD, we assessed whether the brains of individuals who were TREM2 variant carriers who had AD exhibited similar reductions of post-synaptic puncta engulfed in CD68+ phagolysosomes compared to AD cases expressing the common variant of TREM2. We stained prefrontal cortex tissue from late-onset AD TREM2^{R47H} and TREM2^{R62H} individuals and their case-matched controls for Iba1, CD68 and PSD-95. R62H is another TREM2 variant associated with an increased risk for AD (40, 41). Consistent with our mouse data, we detected significantly less PSD-95 puncta engulfed in CD68+ vesicles per microglia in AD TREM2^{R47H} and TREM2^{R62H} brains compared to AD brains with the TREM2^{CV} (Fig. 7 C and D). The detection of lower synaptic phagocytosis by microglia expressing R47H or R62H variants of TREM2 in AD cases confirms the defective synapse elimination by microglia with TREM2 loss-of-function. Taken together, these data suggest that microglia expressing TREM2^{R47H} phagocytose fewer synapses due to lower C1q accumulation in synapses, resulting in neuroprotection in the setting of tauopathy.

Discussion:

TREM2^{R47H} has been associated with higher risk of developing AD. Data from animal models and humans suggests that the likely reason for this effect is that decreased TREM2 function leads to a decreased microglial response to A β deposition, increased A β -associated local neurotoxicity, and an exacerbation of A β -induced tau seeding and spreading (15, 42, 43). However, during the time course of AD, A β aggregation and accumulation in the neocortex occurs over a 15-25-year period prior to symptom onset. Tau aggregation and pathology development in the neocortex does not occur until just a few years prior to the onset of cognitive decline. Thus, while TREM2 signaling may protect against A β -related changes in the brain, the role of TREM2 signaling during the neocortical “tau” phase (symptomatic phase) of AD and in primary tauopathies may not be the same. This is critical to understand as therapeutic targeting of TREM2 may differ depending on the stage of the disease. Our study unveils a role of TREM2 in the control of tau-mediated synaptic elimination and neurodegeneration in the setting of pure tauopathy that may also be relevant to the neocortical tau phase of AD. Surprisingly, we demonstrated that the AD-associated TREM^{R47H} variant strongly reduces the development of brain atrophy, as well as synapse loss in PS19 mice. Importantly, in the presence of TREM^{R47H}, tau phosphorylation was decreased, suggesting that phospho-tau pathogenesis might be influenced TREM2 function. Further analysis revealed decreased microglial activation and reduced expression of several DAM genes in PS19-T2^{R47H} mice. These results indicate that TREM2 contributes to the microglial response to tau pathology or tau-mediated impairment. Importantly, a decrease in phagocytosis of postsynaptic elements by microglia expressing TREM2^{R47H} was detected in PS19 mice and AD patients and can, at least in part, explain the decrease in synaptic damage observed in PS19-T2^{R47H} mice. Finally, we observed that microglia expressing TREM2^{R47H} phagocytose fewer synapses due to lower C1q accumulation in synapses, resulting in neuroprotection in the setting of tauopathy.

While the TREM2^{R47H} variant has been associated with a higher risk of developing AD, we observed delayed progression of phospho-tau pathology and neurodegeneration in the hippocampus of PS19-TREM2^{R47H} mice. Surprisingly, in two previous studies of PS19 mice with complete absence of TREM2, no change in tau pathology has been reported (25, 26). We do not

know the answer to why TREM2^{R47H} decreases some pTau species at 9 months of age compared to TREM2^{CV} in PS19 mice whereas TREM2 deletion did not have this effect compared to mice expressing murine TREM2 (25). However, we can speculate that this dissimilarity results from the slightly different age of the mice used between the two studies or because of the difference between mouse and human TREM2. Indeed, in the Leyns et al. study (25), the PS19 mice expressed mouse TREM2, which may have a slightly different overall effect compared to human TREM2^{CV} used in this study. Unlike studies on PS19 mice, complete deletion of TREM2 in hTau mice exacerbated tau phosphorylation and insolubility (27). Despite the apparent confusion regarding the impact of TREM2 on tau pathology, we hypothesized that reduced tau pathology in PS19-T2^{R47H} mice results from decreased microglial activation. Indeed, in a mouse model of tau propagation using an injection of AAV2/6-SYN1 promoter driving the expression of human P301L tau mutant into the brain, Asai et al. report that depleting microglia dramatically suppressed tau propagation (44). Moreover, microglial activation has been shown to correlate with a deficit in spatial memory and the spread of tau pathology in hTau mice (45). Recently, our lab and others also demonstrated the progression of phosphorylated tau pathology is also driven by microglia in PS19 mice (28, 30). Moreover, the same study by Shi et al. demonstrated that microglial-mediated damage was the leading force driving neurodegeneration in a pure tauopathy mouse model. Similarly, Leyns et al. and Sayed et al. previously reported that complete loss of TREM2 protects against tau-mediated brain atrophy as well as lower microgliosis (25, 26). Importantly, even though we observed decreased tau pathology in PS19-T2^{R47H} mice, the neuroprotective effect by TREM2^{R47H} characterized in this study is likely attributable to reduced microglia-dependent neuronal damage rather than a direct effect on pTau pathology *per se*. Indeed, decreased tau pathology in the piriform cortex has been observed only on p.Thr231 while preserved brain volume, pyramidal layer thickness and synaptic integrity is reported in the piriform cortex of PS19-T2^{R47H} mice as well as a strong reduction of microgliosis. Moreover, Leyns et al. previously reported a neuroprotection induced by TREM2 deletion in PS19 mice without change in tau pathology but with lower microgliosis (25). Thus, diminished microgliosis resulting from the R47H variant of TREM2 seems to explain the brain atrophy attenuation in PS19 mice observed in this study. Because synapse loss is well characterized in mouse models of tauopathies

(29, 46–48), and TREM2 has been shown to play a key role in synaptic pruning during brain development (39), we then hypothesized that TREM2 loss-of-function leads to lower brain atrophy in PS19 mice by inhibiting synaptic phagocytosis by microglia. Indeed, our lab previously reported higher levels of PSD-95, a post-synaptic marker, in PS19-TREM2 KO compared to PS19 mice (25). We confirmed that PS19 mice expressing TREM2^{R47H} have strikingly more pre- and post-synaptic markers, as well as better maintained pre- and post-synaptic interactions compared to PS19-T2^{CV} mice.

While the TREM2^{R47H} protective effect against tau-mediated brain atrophy and synapse loss seems clear in this study, the possible mechanisms underlying this phenomenon are multiple. First, chronic immune activation is known to result in high levels of several pro-inflammatory cytokines such as TNF α or IL1 β that can induce synaptic excitotoxicity (49–52); and we show that PS19-T2^{R47H} mice have a robust reduction in the expression of TNF α and IL1 β , as well as several other pro-inflammatory cytokines compared to PS19-T2^{CV}. Second, as previously mentioned, TREM2 is well known for its functions in promoting microglial cell survival (53) and in cellular phagocytosis (37, 54, 55). Filipello et al. also characterized that TREM2 is essential for microglial-mediated synaptic refinement during the early stages of brain development and that TREM2 deletion resulted in impaired synapse elimination (39). Moreover, a recent study by Sheng et al. reported that TREM2 deficiency ameliorates synaptic deficits in 8-month-old APP/PS1 mice, an amyloid mouse model (56). In PS19-T2^{R47H} mice, we confirmed the reduction of microglial phagocytic properties with fewer CD68+ phagolysosomes within microglia. In addition, a decrease in number of post-synaptic puncta engulfed in CD68+ vesicles was observed not only in PS19-T2^{R47H} mice, but also in AD patients harboring either the R47H mutation or the R62H mutation, another AD-associated TREM2 variant (41, 57, 58). These data suggest that partial loss-of-function induced by AD-associated TREM2 variants might protect against aberrant synaptic phagocytosis by microglia due to chronic inflammation. The impaired phagocytosis of synapses by microglia might also be due to lower C1q accumulation in synapses. C1q, the initiating protein of the classical complement cascade, is increased and associated with synapses before overt amyloid plaque deposition in AD and inhibition of C1q reduces the number of phagocytic microglia, as well as the extent of early synaptic loss in familial AD-mutant hAPP (“J20”)

transgenic mice (59). More recently, Dejanovic et al. (34) reported a striking accumulation of complement C1q in synapses of PS19 mice and AD patients. Moreover, they demonstrated an association of synaptic C1q accumulation with augmented microglial engulfment of synapses and decline of synapse density *in vitro*. Interestingly, we reported that despite more synapses in PS19-T2^{R47H} mice, there is dramatically less C1q opsonized synapsin and PSD-95 puncta detected in the brain of these mice in comparison to PS19-T2^{CV} mice. This is consistent with lower C1q accumulation in synapses of PS19-T2^{R47H} mice compromising the signal for microglia to engulfed them, preserving synaptic density. Importantly, a combination of all these mechanisms resulting from the inhibition of a chronic inflammatory vicious circle remains conceivable here.

Obviously, an evident question emerges from this study: how does TREM2^{R47H} increase the risk of developing AD, but appears protective against tau-mediated synapse loss? The answer might be amyloid, tau, and time-dependent. Recently, we have found that TREM2 deficiency increases amyloid-induced tau spreading (25), which is a phase of AD pathogenesis that precedes the tau-linked neurodegeneration phase of AD. In this study (25), we showed that TREM2 KO or AD-associated TREM2^{R47H} variant reduces microgliosis around A β plaques. Importantly, TREM2 KO and AD-associated TREM2^{R47H} variant strongly promoted tau seeding and spreading in the form of neuritic plaque (NP) tau aggregates. In addition, decreased plaque-associated microgliosis in these mice corresponded with higher peri-plaque A β 42 accumulation and formation of neuritic dystrophy around plaques. These findings demonstrate a critical role for TREM2 in microglia in inhibiting a key element of A β -facilitated tau pathology. Therefore, we hypothesize that AD-associated TREM2 variants increase AD-risk by promoting A β -mediated local toxicity and facilitate tau seeding and spreading in the early pathological stages of the disease. However, in the later stages of the disease (i.e. symptomatic stage) and in primary tauopathies, when substantial tau pathology has developed, AD-associated TREM2 variants might slow down tau-mediated synapse loss in the brain through reduction of synapse phagocytosis by microglia. It is important to note that complete loss of function of TREM2 in humans results in a disease called Nasu-Hakola disease characterized by cerebral degeneration and white matter damage (60, 61). However, partial loss of function of TREM2 as seen with the TREM2^{R47H} mutation in heterozygous or homozygous condition is associated with increased risk for AD (not with Nasu-

Hakola disease) (9, 10, 62). Thus, it may be that decreasing but not ablating TREM2 function during the tau phase of neurodegeneration may result in neuroprotection not only in mouse models but also in humans.

Taken together, we found that TREM2 plays a key role in neurodegeneration in the context of tau pathology. Surprisingly, the AD-associated R47H variant of TREM2 was strongly neuroprotective, probably because of decreased chronic inflammation and decreased synaptic phagocytosis. While research on microglia and TREM2 in AD has largely focused on TREM2 interactions with A β pathology, this study suggests that TREM2 can directly affect tau pathology and tau-mediated neurodegeneration in the brain. This study raises new important questions about targeting TREM2 as a therapeutic approach to treat AD. Indeed, stimulating the TREM2 pathway using antibodies or drugs is thought to be a new promising therapeutic strategy to treat or slowdown AD progression. However, this study suggests that TREM2 exacerbates tau-mediated neurodegeneration in the later stages of the disease when tau pathology is prominent. This study highlights the complexity of using TREM2 as a target to treat AD or a primary tauopathy. Moving forward, it will be important to identify and establish the appropriate therapeutic window using a close monitoring of stage neurodegeneration and inflammation related AD biomarkers to either stimulate or inhibit the TREM2 pathway based on the disease and its stage. This should be possible with the use of fluid and imaging based biomarkers. Importantly, this study revealed for the first time that the AD-associated TREM2^{R47H} variant is protective against tau pathology and tau-mediated neurodegeneration.

Methods

Animals

PS19 transgenic mice expressing human P301S 1N4R mutated tau driven by the PrP promoter were purchased from The Jackson Laboratory (#008169). PS19 mice were backcrossed and maintained on a mouse TREM2 knock-out background (T2KO). PS19-T2KO were crossed to mice that had been engineered using bacterial artificial chromosome (BAC) technology to express human TREM2 with either the common variant (TREM2^{CV}) or the AD-associated R47H variant (TREM2^{R47H}) on a mouse T2KO background (15). These BAC transgenic mice carrying human TREM2 (common variant or R47H variant), TREML1, and TREML2 were back-crossed to Trem2 KO mice to yield mice that express either the common variant or the R47H of human TREM2 in the absence of mouse TREM2. The use of BAC TREM2 models, prohibited the ability to compare littermates with different genotypes in this study. Because of the fact that male PS19 mice at different ages have both greater tau pathology, neurodegeneration, and less variability than female mice (63, 64), only males were used for analysis in this study. All mice were on C57BL/6 background. Animal procedures and experiments were performed under guidelines approved by the Animal Studies Committee at Washington University School of Medicine.

Sample collection

At time of death, mice were anesthetized with i.p. pentobarbital (200 mg/kg). Blood samples were collected in EDTA-treated tubes before cardiac perfusion with with 3 U/mL heparin in cold Dulbecco's PBS. Blood samples were spun down (10 min, 2,000 g, 4°C), and blood plasma was collected. Brains were carefully extracted and cut into two hemispheres. The left hemisphere was collected for immunostaining and fixed in 4% paraformaldehyde overnight before being transferred to 30% sucrose and stored at 4 °C until they were sectioned. Brains were cut coronally into 50-µm sections on a freezing sliding microtome (SM1020R; Leica) and stored in cryoprotectant solution (0.2 M PBS, 15% sucrose, 33% ethylene glycol) at -20 °C until use. The right hemisphere was dissected to isolate the hippocampus and the cortex for biochemical analysis, and the tissue was kept at -80 °C until analyzed.

For electron microscopy, 3 mice per group were anesthetized with i.p. pentobarbital (200 mg/kg) and perfused with 0.1% glutaraldehyde in 4% paraformaldehyde (65). Fifty-micrometer-thick coronal sections of the brain were cut in sodium phosphate buffer using a vibratome (Vibratome series 1000 sectioning system) and stored at -20°C in cryoprotectant until further processing (66).

Volumetric analysis of brains sections

Every sixth brain section (300 μm between sections) starting rostrally at bregma -1.23 mm to the dorsal end of the hippocampus at bregma -2.73 mm were mounted on slides and allowed to dry overnight for each mouse. The following day, mounted sections were stained with 0.1% Sudan Black in 70% ethanol at room temperature for 20 min, then washed in 70% ethanol 3 times for 1 minute. The sections were washed in Milli-Q water and coverslip with Fluoromount (Southern Biotech). Slides were imaged with the NanoZoomer 2.0-HT system (Hamamatsu Photonics) and areas of interest measured using the NDP viewer software (Hamamatsu Photonics). The volume for each region of interest was calculated using the formula: volume = (summary of areas) x 0.3mm.

Neuronal layer thickness measurement

Three sections (bregma -2.0 , -2.4 , and -2.8 mm) per mouse were mounted and allowed to dry overnight. The following day, sections were stained in cresyl violet for 6 min at RT. The slices were then sequentially dehydrated in increasing ethanol concentrations followed by xylene and coverslipped with Cytoseal 60 (Thermo Fisher Scientific, 8310-16). The thickness of the pyramidal cell layer of the piriform cortex and dentate gyrus granular cell layer were measured by drawing a scale perpendicular to the cell layer in all three slices and taking the average value for each mouse.

Brain extraction and tau and pTau ELISA

Half hippocampus was weighed and homogenized using a pestle with 20 μl buffer/1mg tissue (10mM Tris-HCl pH7.4, 0.8M NaCl, 1mM EDTA, 2uM DTT, cOmplete, PhosStop, 10% sucrose). Samples were centrifuged for 10min, 10,000 x g at 4°C . Supernatant was removed and kept on

ice while pellet was re-homogenized in the same volume of buffer with sonicator at 30% amplitude, 1s/1s pulse, for 1min and centrifuged for 10min, 10,000 x g at 4°C. The two supernatants were pooled together and frozen until used. The concentration of tau and pTau were quantified in sandwich ELISA as previously described (42) using Tau-5 (in-house antibody) as the coating antibody and human-specific biotinylated HT7 for detection for tau ELISA and using HJ14.5 (in-house p.Thr181-tau antibody) as the coating antibody and human-specific biotinylated AT8 for detection for pTau ELISA. Briefly, a 96-well half-area plates were coated with 20µg/mL of either HJ14.5 or Tau5 antibodies and incubated at 4°C overnight. The next day, the plate was blocked in 3% BSA (RPI Corp.) in PBS for 1 hour at 37°C. Next, standards peptides and samples were diluted in sample buffer (.25% BSA-PBS, 1x protease inhibitor, 300mM Tris pH 7.4, PBS), loaded onto the plate, and incubated at 4°C overnight. On the third day, 0.3µg/mL of biotinylated AT8 for pTau ELISA (MN1020B ThermoFisher Scientific) or biotinylated HT7 for tau ELISA (MN1000B ThermoFisher Scientific) were applied to the plate for 1.5 hours at 37°C, then Streptavidin-poly-HRP-40 (1/10000 for tau and 1/6000 for pTau) – (Fitzgerald) was applied for 1.5 hours at room temperature. TMB Superslow Substrate solution (Sigma) was added and the plates were read at 650nm on a Biotek plate reader after developing for 30 minutes at room temperature. All samples were run in duplicate.

Immunohistochemistry

For microglial (Iba1, rabbit polyclonal, 1/5000; 019-19741; Wako) and phospho-tau (AT8, mouse monoclonal, 1/500; MN1020B ThermoFisher Scientific - AT180, mouse monoclonal, 1/500; MN1040 – PG5, mouse monoclonal, 1/500; gift from Peter Davies, Feinstein Institutes for Medical Research, Northwell Health, Manhasset, NY, USA) staining, sections were washed three times in TBS for 5 min and blocked in 0.3% hydrogen peroxide for 10 min. After washing, sections were blocked in 3% milk in TBS with 0.25% Triton X-100 (TBSX) for 30 min. Primary antibody was diluted in 3% milk–TBSX, and the sections were incubated in the primary antibody overnight at 4°C. The next day, sections were washed and incubated with secondary diluted in 3% milk–TBSX for 1 h. For AT8 staining, after washing, sections were incubated in ABC elite solution (VectaStain; PK-6100), prepared following manufacturer’s instructions, for 1 h followed by another washing step.

For Iba1, AT180 and PG5 staining, after washing, sections were incubated with HRP-conjugated secondary antibodies for 1 hour at room temperature (111-035-003; Jackson 1/500). Sections were developed in DAB solution (Vector Laboratories; SK4103), washed, and mounted on slides. After drying overnight, the slides were dehydrated in increasing ethanol concentrations followed by xylene and coverslipped with Cytoseal 60 (8310; Thermo Fisher). Slides were scanned on a NanoZoomer 2.0-HT system (Hamamatsu Photonics). Images were further processed and quantified with the use of Fiji software version 1.51. All areas were quantified in 2 to 3 sections (300 μ m apart from each other) per mouse.

Immunofluorescence

Immunofluorescence staining was performed as previously described (36). Briefly, free-floating tissue was placed in 12 well plates with netwell inserts containing PBS. Blocking solution, primary and secondary antibody mixtures were centrifuged at 17,000 g for 5 min just prior to use. Tissue was rinsed 3 \times 5 min in PBS followed by blocking in 20% normal goat serum in PBS for 1 hr at RT. Tissue was then incubated overnight at RT with primary antibodies [CD68 (rat monoclonal, 1/500 MCA1957 AbD SeroTec), Iba1 (goat polyclonal, 1/5000, Abcam Ab5076), PSD-95 (rabbit polyclonal, 1/200, ThermoFisher 51-6900), Synapsin-1/2 (guinea pig polyclonal, 1/500, 106 004 Synaptic systems) and C1q (mouse monoclonal, 1/50, ab71940 abcam) in 10% NGS containing 0.3% Triton X-100 in PBS. The following day, sections were rinsed 3 \times 5 min in PBS followed by incubation in secondary antibodies (ThermoFisher 1/500) in 10% NGS containing 0.3% Triton X-100 in PBS for 4 hr at RT. Sections were mounted, dried at RT, briefly rinsed in distilled water, and then coverslipped. Mounting media (\sim 150 μ L/slide) was prepared the day of use by mixing Tris-MWL 4-88 (Electron Microscopy Sciences #17977-150, Hatfield, PA) with AF300 (Electron Microscopy Sciences #17977-25) in a 9:1 ratio.

Image acquisition for immunofluorescence

Images were acquired on a Zeiss LSM 880 microscope with AiryScan detector (Zeiss, Oberkochen, Germany). Quantification was performed using a semi-automated pipeline based upon MATLAB (Mathworks) and Imaris 9.3.1 software (Bitplane) as previously described (36). Spots were

detected for each channel using an XY size of 0.2 μ m, a Z size of 0.6 μ m, and automated background subtraction. A 0.1 μ m XY and 0.3 μ m Z guard was applied to exclude spots intersecting the edge of the image volume. Synaptic loci were identified using custom Matlab scripts from Sauerbeck (36) to find the nearest neighbor based upon the XYZ centroid of the top 20% brightest puncta. A cut-off of 270 nm pre-to-postsynaptic separation was used to quantify synaptic loci for Fig. 6 from the frequency distribution of pre-to-postsynaptic separations. Complement labeling of synaptic loci was performed with Imaris 9.3.1 software (Bitplane) by creating surface of C1q stain based on a threshold applied to all images and by counting the number of pre- and post-synaptic spots positive for this surface. 3 images per mouse were taken in the polymorphic layer of the piriform cortex for this analysis.

Quantification of confocal images for Iba1 and CD68 was performed on a semi-automated platform using MATLAB and Imaris 9.3.1 software (Bitplane) to create surfaces of each stain based on a threshold applied to all images and co-localize Iba1 and CD68 surfaces to evaluate de volume of CD68+ vesicles within Iba1+ cells. For quantification of the number of PSD-95 puncta engulfed in CD68+ phagolysosomes, the number of PSD-95 puncta previously detected were automatically counted within CD68+ surface per microglia using Imaris 9.3.1 software (Bitplane). 3 to 5 microglia were imaged for each mouse/subject.

Immunofluorescence of human tissue

Paraffin-embedded 8 μ m sections were dewaxed in xylene for 6 minutes twice, followed by rehydration descending ethanol-to-water (100% EtOH twice, 95% EtOH, 90% EtOH, 70% EtOH, 30% EtOH, 10% EtOH, 100% water twice). For antigen retrieval, slides were incubated for 45 minutes in citrate buffer pH6. Slides were incubated in 0.1% Sudan black solution in 70% ethanol for 20 minutes to eliminate autofluorescence. After PBS washes, sections were blocked in 10% normal donkey serum and 0.3% Triton X-100 for 1 hour and then placed in primary antibodies overnight at 4°C in blocking solution: CD68 (mouse monoclonal, 1/100, DAKO M0876), Iba1 (goat polyclonal, 1/500, Abcam Ab5076) and PSD-95 (rabbit polyclonal, 1/200, ThermoFisher 51-6900). The following day, sections were washed, placed in secondary antibodies for 2 hours

(ThermoFisher 1/500), and then washed again 3 times for 20 minutes and mounted. Mounting media was prepared the day of use by mixing Tris-MWL 4-88 (Electron Microscopy Sciences #17977-150, Hatfield, PA) with AF300 (Electron Microscopy Sciences #17977-25) in a 9:1 ratio followed by vortexing and bench top centrifugation to remove bubbles. High precision 1.5H coverglass were used for all experiments. Human samples were obtained from the Alzheimer's Disease Research Center at Washington University (St Louis). TREM2^{R47H} and TREM2^{R62H} AD cases were paired with TREM2^{CV} AD-cases matching age, sex, and *APOE* genotype (Table S1).

Gene expression

We extracted total RNA from mice cortex with the RNeasy Mini kit (Qiagen) and prepared cDNA with the High-Capacity RNA-to-cDNA kit (Applied Biosystems), following manufacturer's instructions. Gene expression analysis was performed using microarray analysis in collaboration with the Genome Technology Access Core at Washington University. Using Taqman probes the relative genes expression was quantitatively measured using Fluidigm Biomark HD with integrated fluidic circuits.

Tissue preparation for electron microscopy

3 mice with the common variant and 2 mice with the R47H mutation were used for electron microscopy. In each animal, brain sections containing the polymorphic layer of the piriform cortex (bregma -1.67 mm to -1.91mm) were selected based on the stereotaxic atlas of Paxinos and Franklin 4th edition. The sections were washed three times 10 minutes with phosphate-buffered saline (PBS, 50 mM, pH 7.4) and then incubated 1 hour in a solution of equal volume of 3% potassium ferrocyanide in phosphate buffer (PB, 0.1M, pH 7.4) and 4% aqueous osmium tetroxide. Following three times 5 minutes washes in PB, tissues were incubated 20 minutes in a thiocarbonylhydrazide solution and washed again three times 5 minutes in double distilled water (ddH₂O). A 30-minute incubation of 2% osmium tetroxide (from 4% stock, diluted in ddH₂O) was then performed. The brain sections were washed three times 5 minutes in ddH₂O and dehydrated with an increasing amount of ethanol (5 minutes wash each): 2x35%, 1x50%, 1x70%, 1x80%, 1x90%, 3x100%. After the dehydration in ethanol, the sections were washed three times 5

minutes in propylene oxide and were emerged overnight in Durcupan resin. The following day, tissues were placed between 2 ACLAR sheets (Electron Microscopy Sciences) covered with a thin layer of resin and placed 3 days at 55°C to polymerize.

Ultramicrotomy and transmission electron microscopy

The polymorphic layer of the piriform cortex was excised from the ACLAR sheet with a razor blade and glued onto a resin block. The tissues were then cut using an ultramicrotome (Leica Ultracut UC7), first with a thickness of 300 nm to confirm the region of interest using toluidine blue, and finally at a thickness of 70 nm. The ultrathin sections were collected onto copper mesh grids. The polymorphic layer was imaged at 80kV using a transmission electron microscope (FEI Tecnai Spirit G2) equipped with a Hamamatsu ORCA-HR digital camera (10 MP). The user was blinded to the experimental conditions during imaging and ultrastructural interpretation. Images of the synaptic neuropil were randomly acquired throughout the region of interest as to avoid bias. 16 to 20 non-overlapping images at a magnification between 6,800X and 13,500X were taken per animal. Overall, between 575 μm^2 and 729 μm^2 of the synaptic neuropil were imaged per animal.

Images were analyzed using the software ImageJ. For the qualitative analysis of synaptic ultrastructure, the following parameters were considered: the presence and size of autophagosomes, the presence of altered mitochondria, the presence of dark dendrites, dendritic spines or axon terminals and the presence of dystrophic synapses. Dark cells (e.g. microglia, neurons) are cells characterized by ultrastructural signs of oxidative stress (endoplasmic reticulum dilation, condensation of the nucleo- and cytoplasm, altered mitochondria) (67, 68) and have been seen previously in pathological conditions, such as AD (69). Axon terminals were recognized by their inclusion of multiple synaptic vesicles. Dendritic spines were recognized and differentiated from dendrites by their size and presence of a post-synaptic density (70). Dark synaptic elements were recognized by their electron-dense cytoplasm (71). Altered mitochondria were distinguished from normal ones by their large increase in size and/or a disruption of their cristae and/or outer membrane structure (72). Dystrophic synapses were defined by the presence of autophagosomes, a reduced number of synaptic vesicles and a

swollen shape (seen as an increase in size and/or electron-lucent content). Autophagosomes were recognized by their circular shape and delineating double membrane (73).

Statistics

Unless otherwise stated, all data were presented as mean \pm SEM. GraphPad Prism 8.0.0 (La Jolla California USA) was used to perform statistical analyses. Gaussian distribution was evaluated using the D'Agostino-Pearson normality test. Statistical analysis was performed using two-tailed Student's unpaired t-test under normal distribution. In case of unequal variances, Welch's correction was used with the Student's unpaired t-test. If samples deviate from normal distribution, statistical analysis was performed using a Mann-Whitney test. For human data, significance was determined by paired two-tailed t-test. $p < 0.05$ was considered significant. *, **, ***, **** symbols indicate significant differences versus PS19-T2CV with $p < 0.05$, $p < 0.01$, $p < 0.001$ and $p < 0.0001$, respectively.

Study approval.

All animal experimental protocols were approved by the Animal Studies Committee at Washington University, Saint Louis, MO, USA.

Author contributions

M.G., M.C., J.D.U., and D.M.H. designed the study. M.G., C.E.G.L., A.D.S., M.K.S.P., M.X., N.K., J.R.S., T.T.K. and M.E.T performed the experiments and analyzed the data. M.G., J.D.U., and D.M.H. wrote the manuscript. All authors discussed the results and commented on the manuscript.

Acknowledgments

This study was supported by the McDonnell Center for Cellular and Molecular Neurobiology (M.G), NIH grant AG047644, the JPB Foundation, the Charles and Helen Schwab Foundation (DMH), and the Edward N. and Della L. Thome Memorial Foundation, Bank of America, N.A.,

Trustee (DMH). Scanning of immunohistochemistry was performed on the NanoZoomer digital pathology system courtesy of the Hope Center Alafi Neuroimaging Laboratory. Confocal data were generated on a Zeiss LSM 880 Airyscan Confocal Microscope, which was purchased with support from the Office of Research Infrastructure Programs (ORIP), a part of the NIH Office of the Director under grant OD021629, and in part with support from the Washington University Center for Cellular Imaging (WUCCI) supported by Washington University School of Medicine, The Children's Discovery Institute of Washington University and St. Louis Children's Hospital (CDI-CORE-2015-505 and CDI-CORE-2019-813) and the Foundation for Barnes-Jewish Hospital (3770 and 4642). We thank the Genome Technology Access Center in the Department of Genetics at Washington University School of Medicine for help with genomic analysis. The Center is partially supported by NCI Cancer Center Support Grant #P30 CA91842 to the Siteman Cancer Center and by ICTS/CTSA Grant# UL1 TR000448 from the National Center for Research Resources (NCRR), a component of the National Institutes of Health (NIH), and NIH Roadmap for Medical Research. This publication is solely the responsibility of the authors and does not necessarily represent the official view of NCRR or NIH. The authors specifically thank Dr. David Blum for his helpful advices during the study.

References

1. Matching T, Test R. Chapter 8 Chapter 8. *Test* 2001;2034:162–173.
2. Holtzman DM, Morris JC, Goate AM. Alzheimer's disease: The challenge of the second century. *Science Translational Medicine* 2011;3(77). doi:10.1126/scitranslmed.3002369
3. Castellani RJ, Rolston RK, Smith MA. Alzheimer disease. *Disease-a-Month* 2010;56(9):484–546.
4. Serrano-Pozo A, Frosch MP, Masliah E, Hyman BT. Neuropathological alterations in Alzheimer disease. *Cold Spring Harbor Perspectives in Medicine* 2011;1(1). doi:10.1101/cshperspect.a006189
5. Leyns CEG, Holtzman DM. Glial contributions to neurodegeneration in tauopathies. *Molecular Neurodegeneration* 2017;12(1). doi:10.1186/s13024-017-0192-x
6. Keren-Shaul H et al. A Unique Microglia Type Associated with Restricting Development of Alzheimer's Disease. *Cell* 2017;169(7):1276-1290.e17.
7. Krasemann S et al. The TREM2-APOE Pathway Drives the Transcriptional Phenotype of Dysfunctional Microglia in Neurodegenerative Diseases. *Immunity* 2017;47(3):566-581.e9.
8. Zhang ZG, Li Y, Ng CT, Song YQ. Inflammation in Alzheimer's Disease and Molecular Genetics: Recent Update. *Archivum Immunologiae et Therapiae Experimentalis* 2015;63(5):333–344.
9. Guerreiro R et al. TREM2 variants in Alzheimer's disease. *New England Journal of Medicine* 2013;368(2):117–127.
10. Jonsson T et al. Variant of TREM2 associated with the risk of Alzheimer's disease. *New England Journal of Medicine* 2013;368(2):107–116.
11. Schmid CD et al. Heterogeneous expression of the triggering receptor expressed on myeloid cells-2 on adult murine microglia. *Journal of Neurochemistry* 2002;83(6):1309–1320.
12. Bouchon A, Hernández-Munain C, Cella M, Colonna M. A DAP12-mediated pathway regulates expression of CC chemokine receptor 7 and maturation of human dendritic cells. *Journal of Experimental Medicine* 2001;194(8):1111–1122.
13. Gratuze M, Leyns CEG, Holtzman DM. New insights into the role of TREM2 in Alzheimer's disease. *Molecular Neurodegeneration* 2018;13(1). doi:10.1186/s13024-018-0298-9
14. Wang Y et al. TREM2 lipid sensing sustains the microglial response in an Alzheimer's disease model. *Cell* 2015;160(6):1061–1071.
15. Song WM et al. Humanized TREM2 mice reveal microglia-intrinsic and -extrinsic effects of R47H polymorphism. *Journal of Experimental Medicine* 2018;215(3):745–760.
16. Ulrich JD et al. Altered microglial response to A β plaques in APPPS1-21 mice heterozygous for TREM2 [Internet]. *Molecular Neurodegeneration* 2014;9(1):20.
17. Jay TR et al. TREM2 deficiency eliminates TREM2+ inflammatory macrophages and ameliorates pathology in Alzheimer's disease mouse models. *Journal of Experimental Medicine* 2015;212(3):287–295.
18. Cheng-Hathaway PJ et al. The Trem2 R47H variant confers loss-of-function-like phenotypes in Alzheimer's disease. *Molecular Neurodegeneration* 2018;13(1). doi:10.1186/s13024-018-0262-8
19. Long JM, Holtzman DM. Alzheimer Disease: An Update on Pathobiology and Treatment Strategies. *Cell* 2019;179(2):312–339.

20. Piccio L et al. Cerebrospinal fluid soluble TREM2 is higher in Alzheimer disease and associated with mutation status. *Acta Neuropathologica* 2016;131(6):925–933.
21. Suárez-Calvet M et al. sTREM 2 cerebrospinal fluid levels are a potential biomarker for microglia activity in early-stage Alzheimer’s disease and associate with neuronal injury markers [Internet]. *EMBO Molecular Medicine* 2016;8(5):466–476.
22. Lill CM et al. The role of TREM2 R47H as a risk factor for Alzheimer’s disease, frontotemporal lobar degeneration, amyotrophic lateral sclerosis, and Parkinson’s disease [Internet]. *Alzheimer’s and Dementia* 2015;11(12):1407–1416.
23. Cruchaga C et al. GWAS of cerebrospinal fluid tau levels identifies risk variants for alzheimer’s disease [Internet]. *Neuron* 2013;78(2):256–268.
24. Buerger K et al. CSF phosphorylated tau protein correlates with neocortical neurofibrillary pathology in Alzheimer’s disease. [Internet]. *Brain : a journal of neurology* 2006;129(Pt 11):3035–41.
25. Leyns CEG et al. TREM2 deficiency attenuates neuroinflammation and protects against neurodegeneration in a mouse model of tauopathy. *Proceedings of the National Academy of Sciences of the United States of America* 2017;114(43):11524–11529.
26. Sayed FA et al. Differential effects of partial and complete loss of TREM2 on microglial injury response and tauopathy. *Proceedings of the National Academy of Sciences of the United States of America* 2018;115(40):10172–10177.
27. Bemiller SM et al. TREM2 deficiency exacerbates tau pathology through dysregulated kinase signaling in a mouse model of tauopathy. *Molecular Neurodegeneration* 2017;12(1). doi:10.1186/s13024-017-0216-6
28. Shi Y et al. Microglia drive APOE-dependent neurodegeneration in a tauopathy mouse model. *The Journal of experimental medicine* 2019;216(11):2546–2561.
29. Yoshiyama Y et al. Synapse Loss and Microglial Activation Precede Tangles in a P301S Tauopathy Mouse Model. *Neuron* 2007;53(3):337–351.
30. Mancuso R et al. CSF1R inhibitor JNJ-40346527 attenuates microglial proliferation and neurodegeneration in P301S mice. *Brain* 2019;142(10):3243–3264.
31. Deming Y et al. The MS4A gene cluster is a key modulator of soluble TREM2 and Alzheimer’s disease risk. *Science Translational Medicine* 2019;11(505). doi:10.1126/scitranslmed.aau2291
32. Liddel SA et al. Neurotoxic reactive astrocytes are induced by activated microglia. *Nature* 2017;541(7638):481–487.
33. Shi Y et al. ApoE4 markedly exacerbates tau-mediated neurodegeneration in a mouse model of tauopathy. *Nature* 2017;549(7673):523–527.
34. Dejanovic B et al. Changes in the Synaptic Proteome in Tauopathy and Rescue of Tau-Induced Synapse Loss by C1q Antibodies. *Neuron* 2018;100(6):1322-1336.e7.
35. Collman F et al. Mapping synapses by conjugate light-electron array tomography. *Journal of Neuroscience* 2015;35(14):5792–5807.
36. Sauerbeck AD et al. SEQUIN Multiscale Imaging of Mammalian Central Synapses Reveals Loss of Synaptic Connectivity Resulting from Diffuse Traumatic Brain Injury [Internet]. *Neuron* 2020;0(0). doi:10.1016/j.neuron.2020.04.012
37. Takahashi K, Rochford CDP, Neumann H. Clearance of apoptotic neurons without inflammation by microglial triggering receptor expressed on myeloid cells-2. *Journal of Experimental Medicine* 2005;201(4):647–657.

38. Hsieh CL et al. A Role for TREM2 Ligands in the Phagocytosis of Apoptotic Neuronal Cells by Microglia doi:10.1111/j.1471-4159.2009.06042.x
39. Filipello F et al. The Microglial Innate Immune Receptor TREM2 Is Required for Synapse Elimination and Normal Brain Connectivity [Internet]. *Immunity* 2018;48(5):979-991.e8.
40. Chih Jin S et al. Coding variants in TREM2 increase risk for Alzheimer's disease doi:10.1093/hmg/ddu277
41. Sims R et al. Rare coding variants in PLCG2, ABI3, and TREM2 implicate microglial-mediated innate immunity in Alzheimer's disease [Internet]. *Nature Genetics* 2017;49(9):1373-1384.
42. Leyns CEG et al. TREM2 function impedes tau seeding in neuritic plaques. *Nature Neuroscience* 2019;22(8):1217-1222.
43. Zhou Y et al. Human and mouse single-nucleus transcriptomics reveal TREM2-dependent and TREM2-independent cellular responses in Alzheimer's disease. *Nature Medicine* 2020;26(1):131-142.
44. Asai H et al. Depletion of microglia and inhibition of exosome synthesis halt tau propagation. *Nature Neuroscience* 2015;18(11):1584-1593.
45. Maphis N et al. Reactive microglia drive tau pathology and contribute to the spreading of pathological tau in the brain. *Brain* 2015;138(6):1738-1755.
46. van Olst L et al. Microglial activation arises after aggregation of phosphorylated-tau in a neuron specific P301S tauopathy mouse model.. *Neurobiology of Aging* [published online ahead of print: January 10, 2020]; doi:10.1016/j.neurobiolaging.2020.01.003
47. Hoffmann NA, Dorostkar MM, Blumenstock S, Goedert M, Herms J. Impaired plasticity of cortical dendritic spines in P301S tau transgenic mice. *Acta Neuropathologica Communications* 2014;2(1):82.
48. Kopeikina KJ et al. Synaptic alterations in the rTg4510 mouse model of tauopathy. [Internet]. *The Journal of comparative neurology* 2013;521(6):1334-53.
49. Zhao J, O'Connor T, Vassar R. The contribution of activated astrocytes to A β production: Implications for Alzheimer's disease pathogenesis. *Journal of Neuroinflammation* 2011;8. doi:10.1186/1742-2094-8-150
50. Becker D, Zahn N, Deller T, Vlachos A. Tumor necrosis factor alpha maintains denervation-induced homeostatic synaptic plasticity of mouse dentate granule cells. *Frontiers in Cellular Neuroscience* 2013;7(DEC). doi:10.3389/fncel.2013.00257
51. Tachida Y et al. Interleukin-1 β up-regulates TACE to enhance α -cleavage of APP in neurons: Resulting decrease in A β production. *Journal of Neurochemistry* 2008;104(5):1387-1393.
52. Kitazawa M et al. Blocking IL-1 Signaling Rescues Cognition, Attenuates Tau Pathology, and Restores Neuronal β -Catenin Pathway Function in an Alzheimer's Disease Model. *The Journal of Immunology* 2011;187(12):6539-6549.
53. Zheng H et al. TREM2 promotes microglial survival by activating wnt/ β -catenin pathway [Internet]. *Journal of Neuroscience* 2017;37(7):1772-1784.
54. Kawabori M et al. Triggering receptor expressed on myeloid cells 2 (TREM2) deficiency attenuates phagocytic activities of microglia and exacerbates ischemic damage in experimental stroke. *Journal of Neuroscience* 2015;35(8):3384-3396.
55. Atagi Y et al. Apolipoprotein E is a ligand for triggering receptor expressed on myeloid cells 2 (TREM2). *Journal of Biological Chemistry* 2015;290(43):26043-26050.

56. Sheng L et al. Microglial Trem2 induces synaptic impairment at early stage and prevents amyloidosis at late stage in APP/PS1 mice. *FASEB journal : official publication of the Federation of American Societies for Experimental Biology* 2019;33(9):10425–10442.
57. Song W et al. Alzheimer's disease-associated TREM2 variants exhibit either decreased or increased ligand-dependent activation. *Alzheimer's and Dementia* 2017;13(4):381–387.
58. Jin SC et al. Coding variants in TREM2 increase risk for Alzheimer's disease. *Human Molecular Genetics* 2014;23(21):5838–5846.
59. Hong S et al. Complement and microglia mediate early synapse loss in Alzheimer mouse models. *Science* 2016;352(6286):712–716.
60. Paloneva J et al. Mutations in two genes encoding different subunits of a receptor signaling complex result in an identical disease phenotype. *American Journal of Human Genetics* 2002;71(3):656–662.
61. Bianchin MM et al. Nasu-Hakola Disease (Polycystic Lipomembranous Osteodysplasia with Sclerosing Leukoencephalopathy-PLOSL): A Dementia Associated with Bone Cystic Lesions. From Clinical to Genetic and Molecular Aspects. *Cellular and Molecular Neurobiology* 2004;24(1):1–24.
62. Slattery CF et al. R47H TREM2 variant increases risk of typical early-onset Alzheimer's disease but not of prion or frontotemporal dementia. *Alzheimer's and Dementia* 2014;10(6):602-608.e4.
63. Zhang B et al. The microtubule-stabilizing agent, epothilone D, reduces axonal dysfunction, neurotoxicity, cognitive deficits, and alzheimer-like pathology in an interventional study with aged tau transgenic mice. *Journal of Neuroscience* 2012;32(11):3601–3611.
64. Yanamandra K et al. Anti-tau antibodies that block tau aggregate seeding invitro markedly decrease pathology and improve cognition in vivo. *Neuron* 2013;80(2):402–414.
65. Ligorio M, Descarries L, Warren RA. Cholinergic innervation and thalamic input in rat nucleus accumbens. *Journal of Chemical Neuroanatomy* 2009;37(1):33–45.
66. Tremblay ME, Riad M, Majewska A. Preparation of mouse brain tissue for immunoelectron microscopy. *Journal of Visualized Experiments* [published online ahead of print: 2010];(41). doi:10.3791/2021
67. Bisht K et al. Dark microglia: A new phenotype predominantly associated with pathological states. *Glia* 2016;64(5):826–839.
68. Tremblay MÈ, Zettel ML, Ison JR, Allen PD, Majewska AK. Effects of aging and sensory loss on glial cells in mouse visual and auditory cortices. *GLIA* 2012;60(4):541–558.
69. el Hajj H et al. Ultrastructural evidence of microglial heterogeneity in Alzheimer's disease amyloid pathology [Internet]. *Journal of Neuroinflammation* 2019;16(1):87.
70. The fine structure of the nervous system: The neurons and supporting cells, by Alan Peters, Sanford L. Palay, and Henry Def. Webster, 395 pp, illustrated, \$33.00, W. B. Saunders Company, Philadelphia, 1976 [Internet]. *Annals of Neurology* 1978;4(6):588–588.
71. Johnson JE. The occurrence of dark neurons in the normal and deafferentated lateral vestibular nucleus in the rat - Observations by light and electron microscopy. *Acta Neuropathologica* 1975;31(2):117–127.
72. St-Pierre MK, Bordeleau M, Tremblay MÈ. Visualizing Dark Microglia. In: *Methods in Molecular Biology*. Humana Press Inc.; 2019:97–110

73. Smith PY et al. MiR-132/212 deficiency impairs tau metabolism and promotes pathological aggregation in vivo. *Human Molecular Genetics* 2015;24(23):6721–6735.

Figures and figure legends

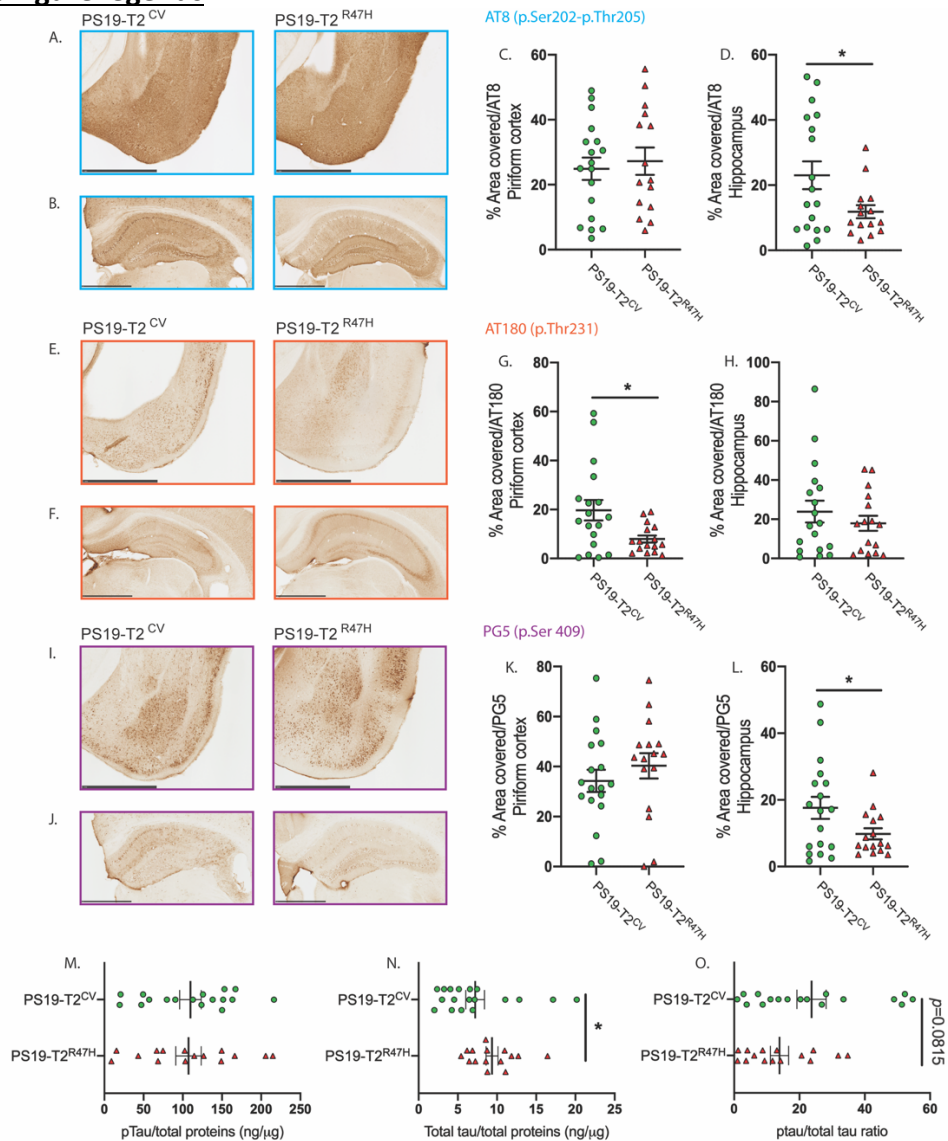


Figure 1: R47H variant of TREM2 attenuates tau pathology in 9-month-old PS19 mice. Representative images of pTau staining (AT8, AT180 and PG5) in the piriform cortex (A, E, I) and hippocampus (B, F, J) from 9-month-old PS19-T2^{CV} and PS19-T2^{R47H} mice. (Scale bars: 1 mm). Quantification of the percent area covered by pTau staining (AT8, AT180 and PG5) in the piriform cortex (C, G, K) and hippocampus (D, H, L). Data are presented as mean \pm SEM. Significance was determined using an unpaired, two-tailed Mann Whitney's test due to the nonparametric data set except for PG5 staining in the hippocampus where an unpaired, two-tailed *t* test with Welch's correction was used due to significantly different variances. Significance was defined as * $p < 0.05$ (PS19-T2^{CV}, $n = 18$ and PS19-T2^{R47H} $n = 15/16$). ELISA results showing concentrations of pTau (p.Ser202-Thr205 and p.Thr181) and total tau and pTau/total tau ratio in the hippocampus were quantified using a human-tau (htau) specific sandwich ELISA to measure pTau (L), total tau (M) and pTau/total tau ratio (L). pTau and total tau (L and M) were normalized to total protein concentration. Data are presented as mean \pm SEM. Significance was determined by an unpaired, two-tailed Student's *t* test except for total tau where an unpaired, two-tailed Mann Whitney's test was used due to the nonparametric data set except. Significance was defined as * $p < 0.05$ (PS19-T2^{CV}, $n = 17$ and PS19-T2^{R47H} $n = 15$).

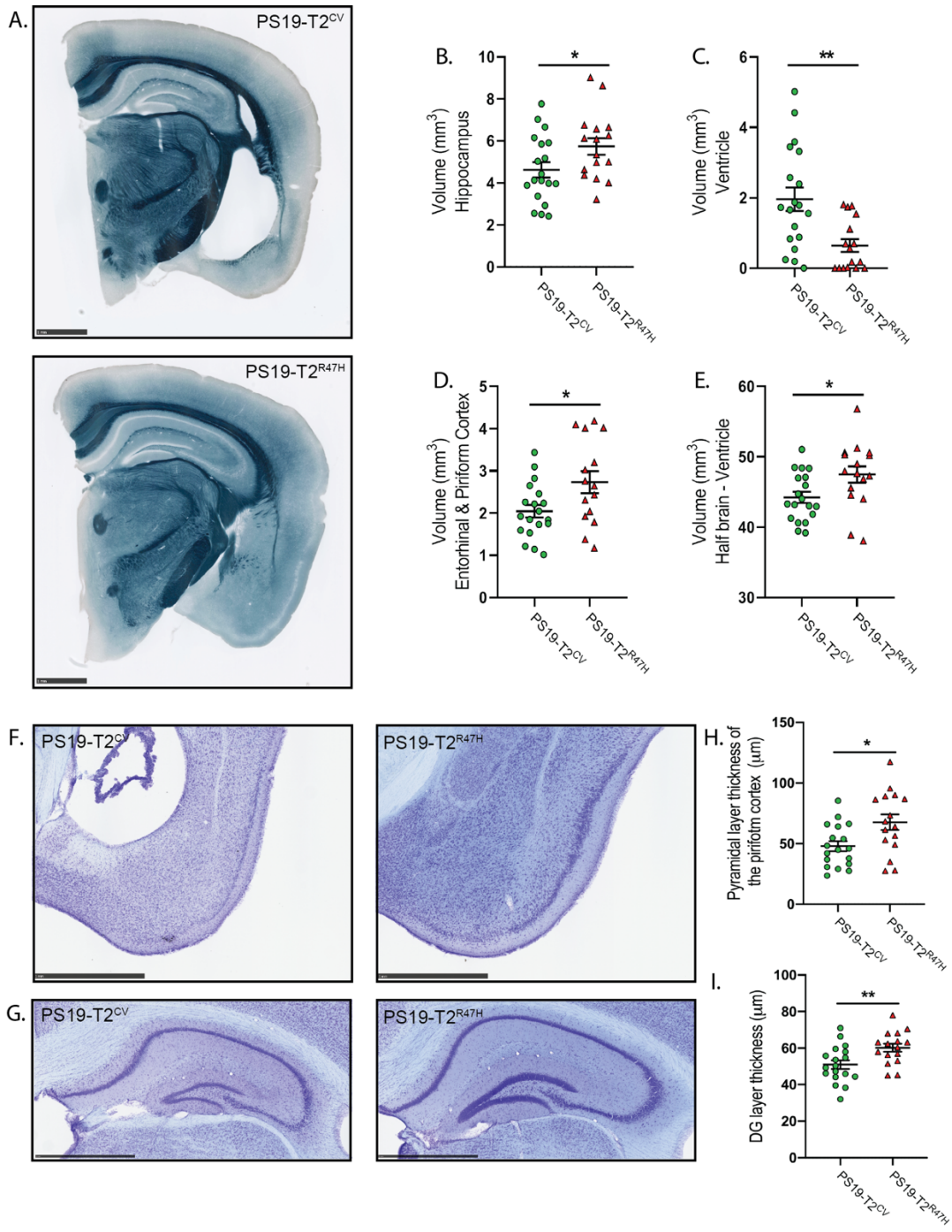


Figure 2: R47H variant of TREM2 decreases neurodegeneration in 9-month-old PS19 mice. Representative images of PS19-T2^{CV} and PS19-T2^{R47H} brain sections stained with Sudan black at 9 months of age (A) (Scale bars, 1 mm). Quantification of the average volume of the hippocampus (B), ventricles (C), entorhinal and piriform cortex (E) and half brain minus ventricle (F). Thickness of the pyramidal layer of the piriform cortex (F and H) and the granule cell layer of the dentate gyrus (G and I) in 9-month-old mice with cresyl violet staining. Data are presented as mean ± SEM. Significance was determined by an unpaired, two-tailed Student's t test. Significance was defined as * $p < 0.05$ and ** $p < 0.01$ (9-month-old: PS19-T2^{CV}, n=18/19 and PS19-T2^{R47H} n=16).

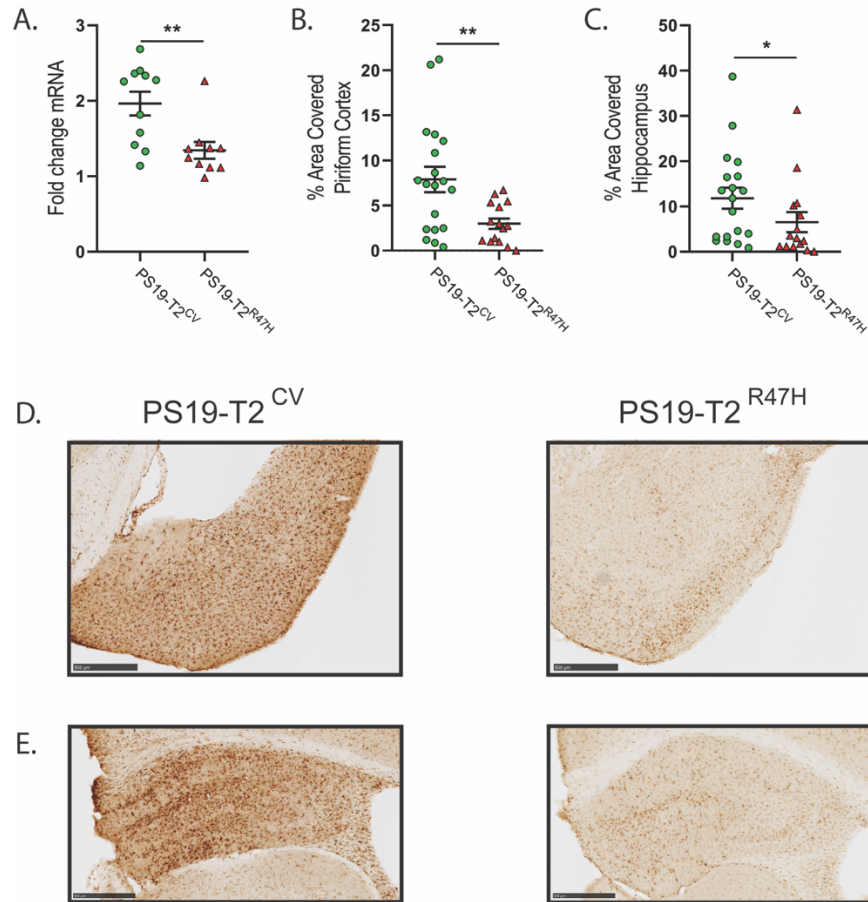


Figure 3: R47H variant of TREM2 decreases microgliosis in 9-month-old PS19 mice. Expression of microglial Iba1 marker in the cortex of 9-month-old PS19-T2^{CV} and PS19-T2^{R47H} mice (A) (PS19-T2^{CV}, n=11 and PS19-T2^{R47H} n=10). Quantification of the percent area covered by Iba1 staining in the piriform cortex (B) and hippocampus (C) (PS19-T2^{CV}, n=19 and PS19-T2^{R47H} n=18). Representative images of Iba1 staining in the piriform cortex (D) and hippocampus (E) from PS19-T2^{CV} and PS19-T2^{R47H} mice. (Scale bars: 0.5 mm). Data is presented as mean \pm SEM. Significance was determined using an unpaired, two-tailed Mann Whitney's test due to the nonparametric data set. Significance was defined as * p <0.05 and ** p < 0.01.

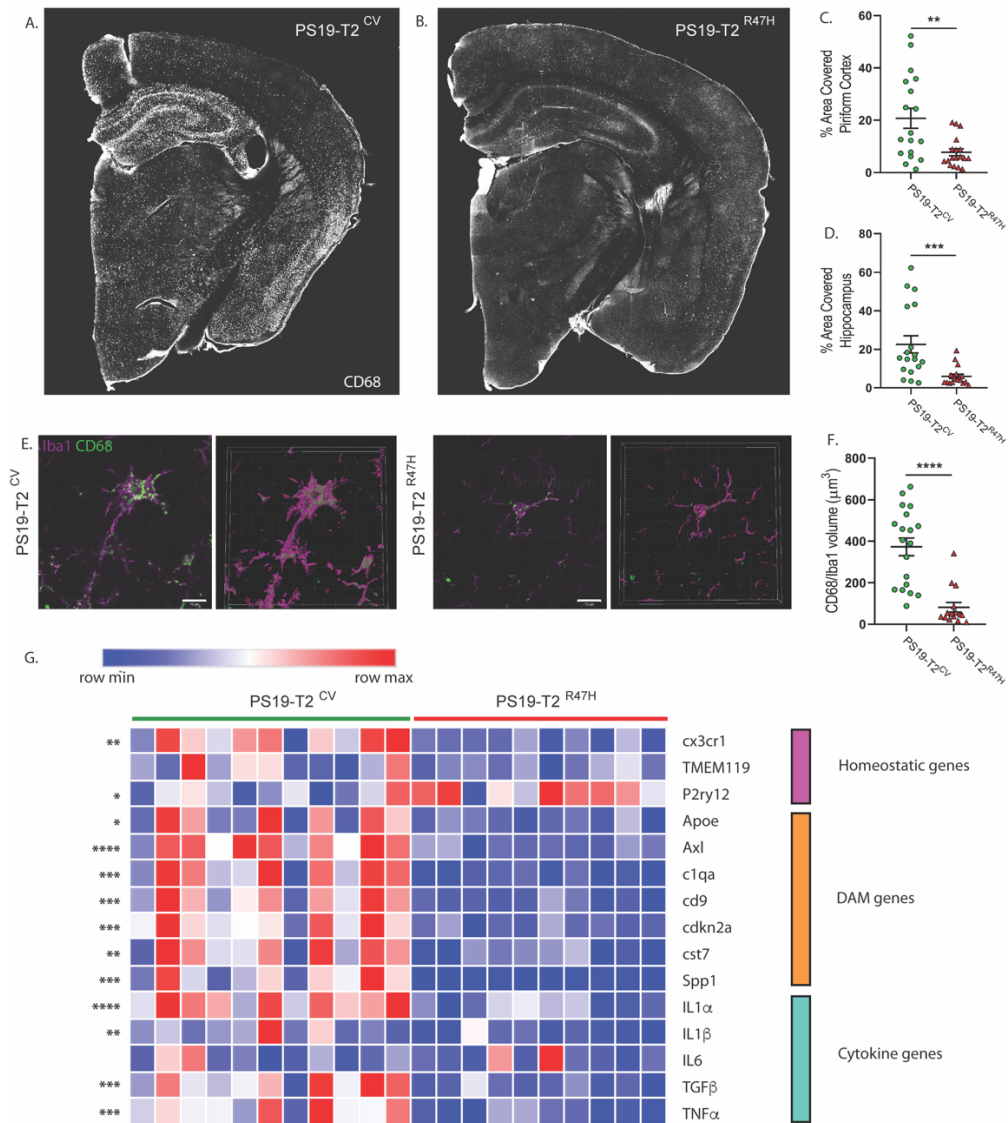


Figure 4: Reduced microglial activation and inflammatory gene expression in 9-month-old PS19-T2^{R47H} vs. PS19-T2^{CV} mice. Representative images of CD68 staining from 9-month-old PS19-T2^{CV} (A) and PS19-T2^{R47H} (B) brains. Quantification of the percent area covered by CD68 staining in the piriform cortex (C) and hippocampus (D) (PS19-T2^{CV}, n=18 and PS19-T2^{R47H}, n=18). Confocal images and 3D reconstruction of CD68⁺ structures within Iba1⁺ microglia in PS19-T2^{CV} (E) and PS19-T2^{R47H} (Scale bar, 10 μm). Quantification (F) of CD68⁺ structures per Iba1 volume. (PS19-T2^{CV}, n=19 and PS19-T2^{R47H} n=15). Data are presented as mean ± SEM. Significance was determined using an unpaired, two-tailed Mann Whitney's test due to the nonparametric data set. Significance was defined as ***p*<0.01, *** *p*<0.001 and *****p*<0.0001. (G) Heatmap analysis for microglial gene expression in 9-month-old PS19-T2^{CV} and PS19-T2^{R47H} piriform cortex region generated by hierarchical genes clustering based on genotypes (DAM genes: Disease-associated microglia genes). For IL1α, P2ry12 and TNFα, significance was determined by an unpaired, two-tailed Student's *t* test. For Apoe, cst7, IL1β, IL6, significance was determined using an unpaired, two-tailed Mann Whitney's test due to the nonparametric data set. For all other analysis, significance was determined by an unpaired, two-tailed *t* test with Welch's correction due to significantly different variances. Significance was defined as **p*< 0.05, ***p*<0.01, *** *p*<0.001 and *****p*< 0.0001 (PS19-T2^{CV}, n=11 and PS19-T2^{R47H} n=10).

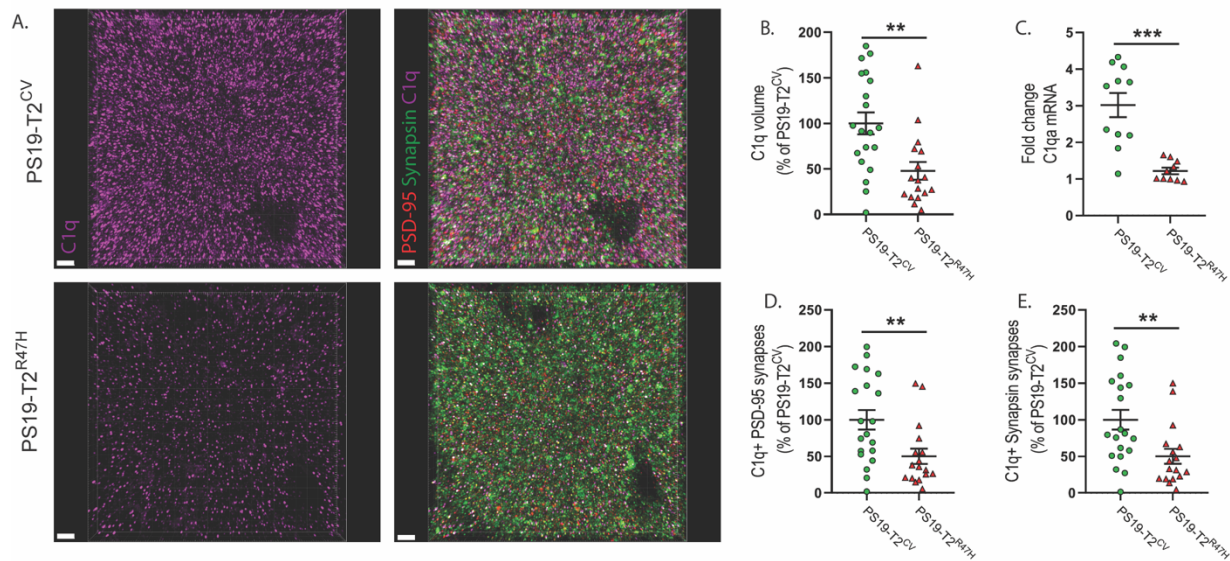


Figure 5: R47H variant of TREM2 lowers C1q⁺ synaptic markers in 9-month-old PS19 mice. Representative images from confocal analysis of pre- (Synapsin in green), postsynaptic (PSD-95 in red) marker and C1q (purple) of 9-month-old PS19-T2^{CV} and PS19-T2^{R47H} piriform cortex (A) (Scale bars, 3 μ m). Quantification of the percent of C1q volume (B), C1q⁺ PSD-95 puncta number (D) and C1q⁺ Synapsin puncta number (E) (PS19-T2^{CV}, n=20 and PS19-T2^{R47H} n=17). Expression of cortical C1qa mRNA in 9-month-old PS19-T2^{CV} and PS19-T2^{R47H} mice (C) (PS19-T2^{CV}, n=11 and PS19-T2^{R47H} n=10). Data are presented as mean \pm SEM. Significance was determined using an unpaired, two-tailed Mann Whitney's test due to the nonparametric data set. Significance was defined as ** p < 0.01 and *** p < 0.001.

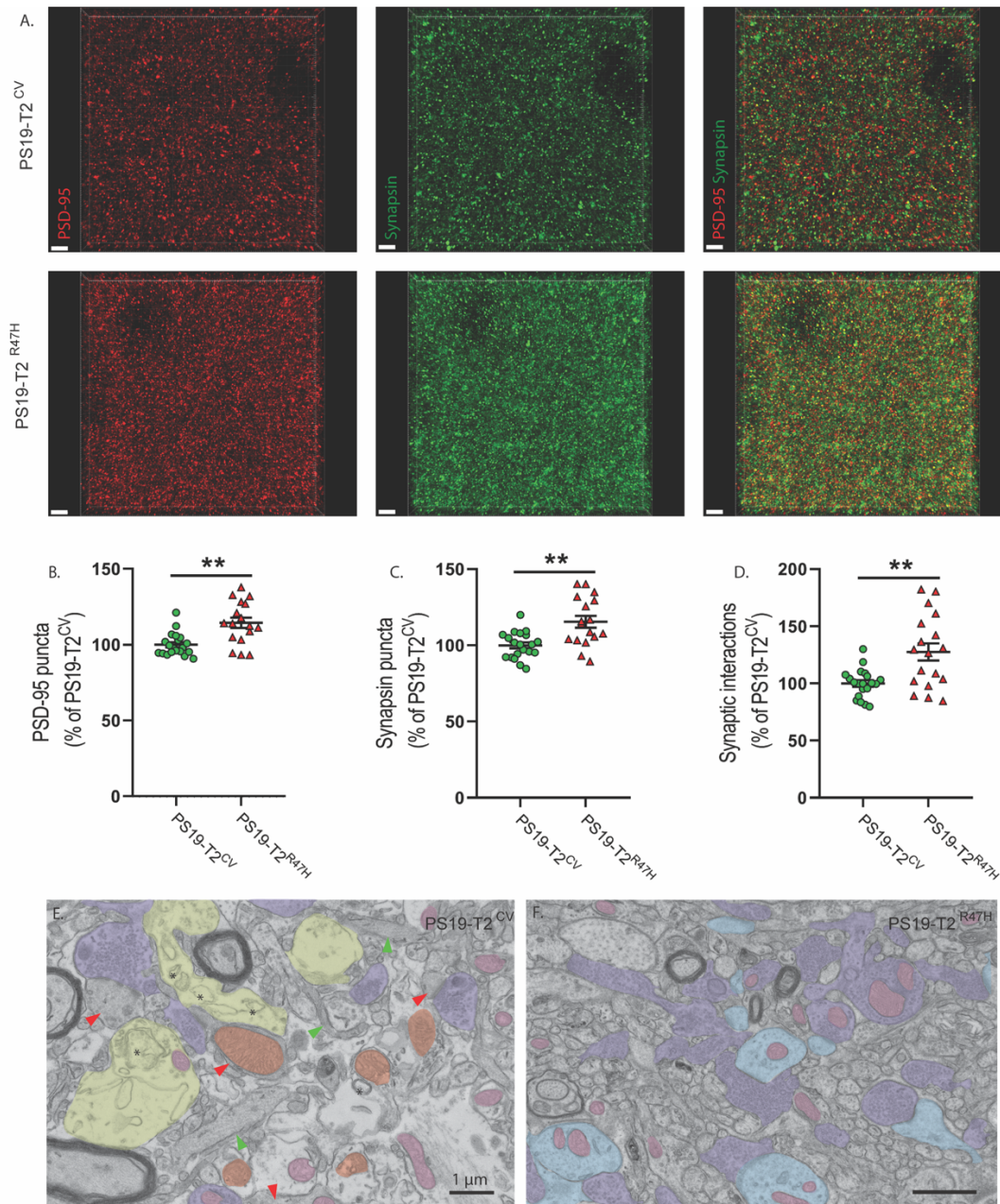


Figure 6: R47H variant of TREM2 reduces synapse loss in 9-month-old PS19 mice. Representative images from confocal analysis of pre- (synapsin in green) and postsynaptic (PSD-95 in red) marker of 9-month-old PS19-T2^{CV} and PS19-T2^{R47H} piriform cortex (A) (Scale bars, 3 μm). Quantification of puncta numbers from PSD-95 (B) and synapsin (C) staining and SEQUIN quantification of synaptic loci (D). Data are presented as mean ± SEM. A Mann–Whitney test was used to determine statistical significance for PSD-95 puncta due to the nonparametric data set. For all other graphs, significance was determined by an unpaired, two-tailed *t* test with Welch’s correction due to significantly different variances. Significance was defined as ***p* < 0.01 (PS19-T2^{CV}, *n*=20 and PS19-T2^{R47H} *n*=17). Electron microscopic images of (E) a PS19-T2^{CV} mouse and in (F) a PS19-T2^{R47H} mouse. Images were taken at 9300x and 6800X, respectively, using a FEI Tecnai Spirit G2 transmission electron microscope. Purple = healthy terminal axons, light blue = healthy dendritic spines, light pink = healthy mitochondria, yellow = dystrophic terminal axons, orange = altered mitochondria, red arrow = dark dendritic spines, green arrow = dark dendrite, * = autophagosomes.

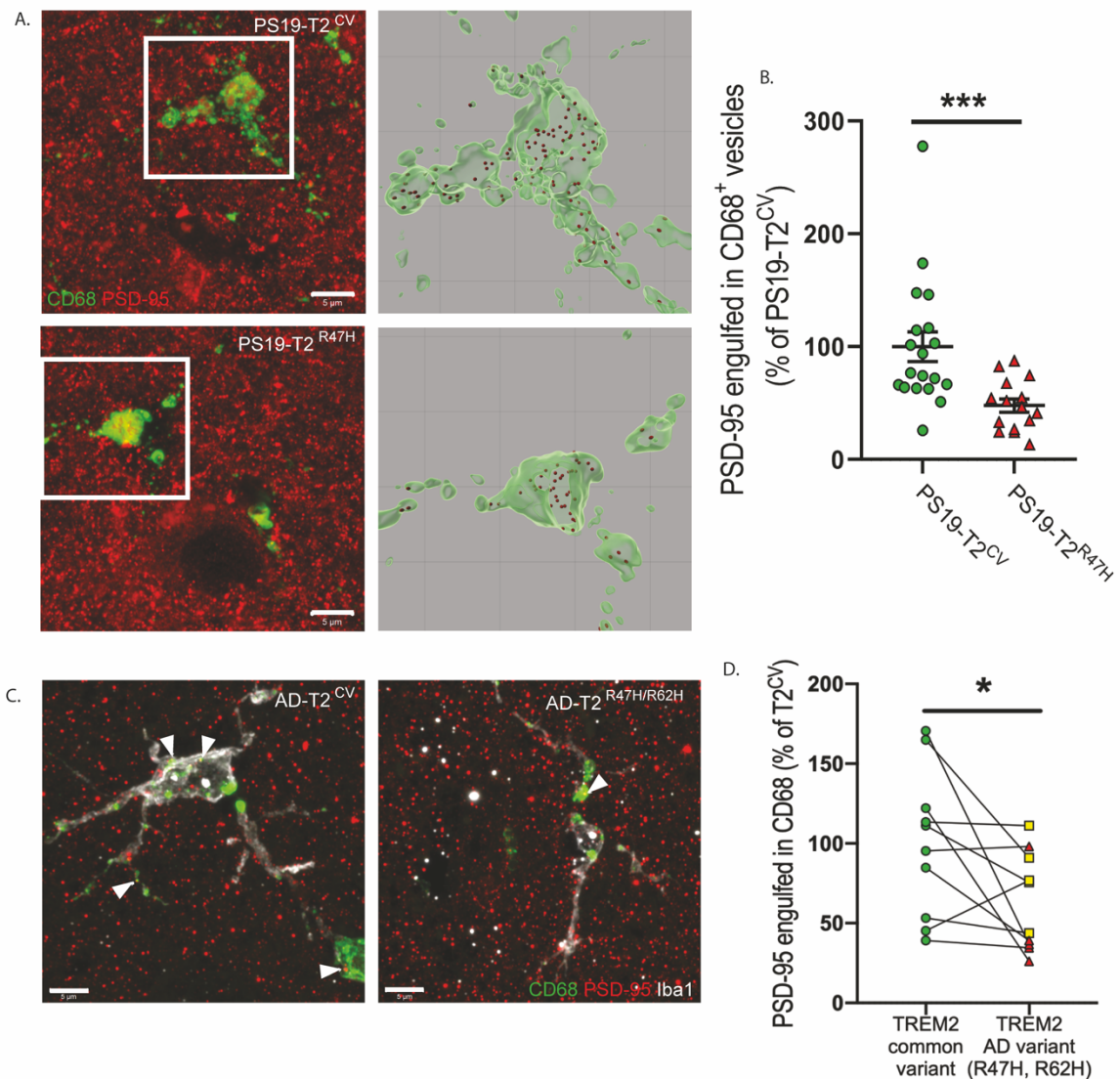


Figure 7: R47H variant of TREM2 alters synapse engulfment by microglia in 9-month-old PS19 mice and human TREM2 variant carriers (R47H and R62H). Representative confocal images and relative 3D surface rendering showing volume reconstruction of CD68 (green) and engulfed PSD95 puncta (red), detected within microglial CD68+ structures of 9-month-old PS19-T2^{CV} and PS19-T2^{R47H} piriform cortex (A) (Scale bars, 5 μm). Quantification of engulfed PSD95 puncta within CD68+ vesicles per microglia (B). Data are presented as mean ± SEM. Significance was determined using an unpaired, two-tailed Mann Whitney's test due to the nonparametric data set. Significance was defined as ****p* < 0.001. (PS19-T2^{CV}, *n*=19 and PS19-T2^{R47H} *n*=15) Representative image from confocal analysis of microglia (white), CD68 (green) and engulfed PSD95 puncta (red), detected within microglial CD68+ structures in TREM2^{R47H} (red triangle) and TREM2^{R62H} (yellow square) AD patients and case-matched TREM2^{CV} AD-controls (C) (Scale bar; 5 μm). Quantification of engulfed PSD95 puncta within CD68 positive structures (arrowheads) per microglia (D). Data are presented as mean ± SEM. Significance determined by paired, two-sided t-test. Significance was defined as **p* < 0.05. (AD-TREM2^{CV}, *n*=9, AD-TREM2^{R47H} *n*=5 and AD-TREM2^{R62H} *n*=5).

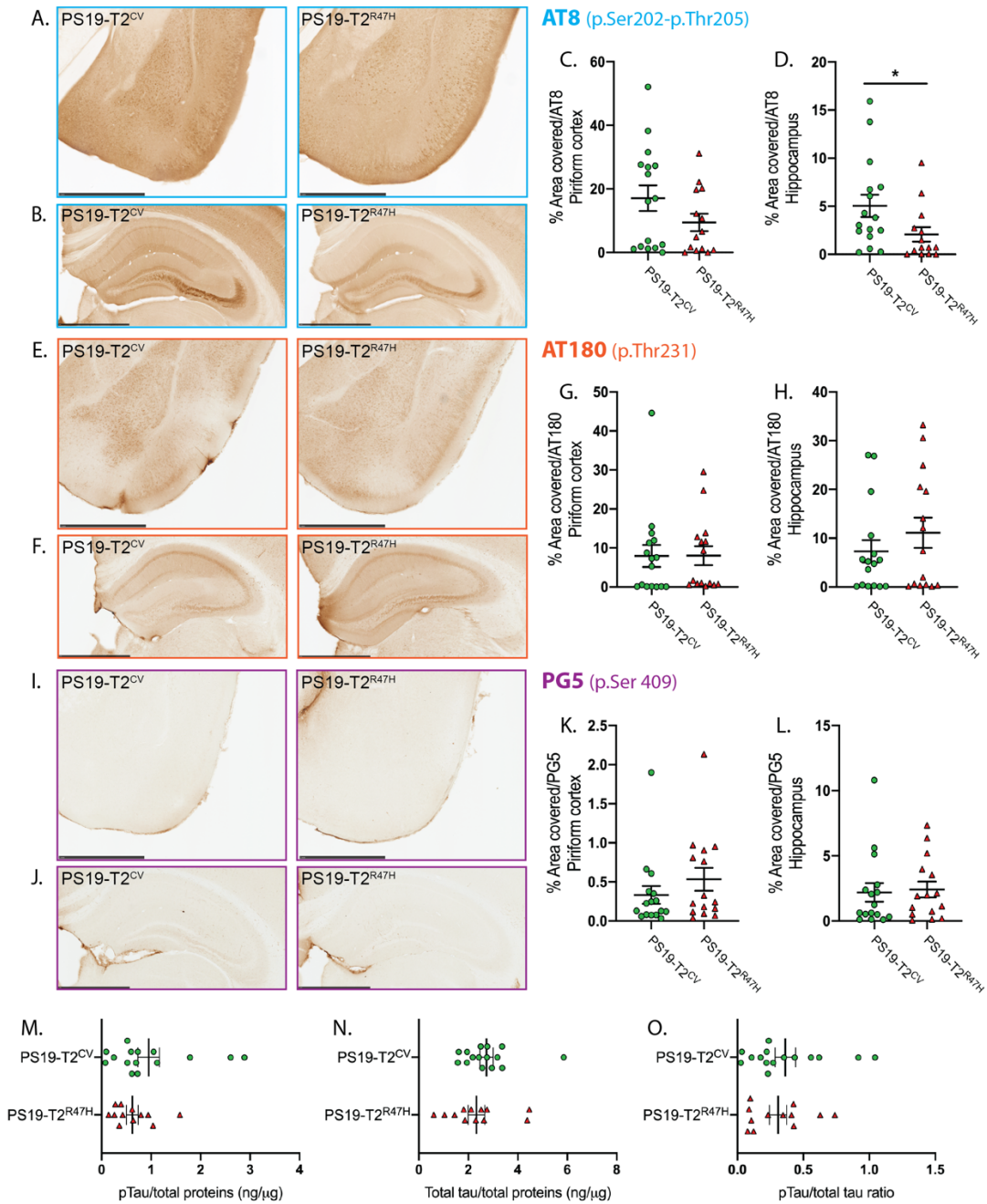


Figure S1: Impact of R47H variant of TREM2 on tau pathology in 3-month-old PS19 mice. Representative images of pTau staining (AT8, AT180 and PG5) in the piriform cortex (A, E, I) and hippocampus (B, F, J) from PS19-T2^{CV} and PS19-T2^{R47H} mice. (Scale bars: 1 mm). Quantification of the percent area covered by pTau staining (AT8, AT180 and PG5) in the piriform cortex (C, G, K) and hippocampus (D, H, L). Data are presented as mean \pm SEM. Significance was determined using an unpaired, two-tailed Mann Whitney's test due to the nonparametric data set. Significance was defined as $*p < 0.05$ (PS19-T2^{CV}, $n=16$ and PS19-T2^{R47H} $n=14/15$). ELISA results showing concentrations of pTau (p.Ser202-Thr205 and p.Thr181) and total tau and pTau/total tau ratio in the hippocampus were quantified using a human-tau (htau) specific sandwich ELISA to measure pTau (L), total tau (M) and pTau/total tau ratio (O). pTau and total tau (L and M) were normalized on total protein concentration. Data are presented as mean \pm SEM. Significance was determined by an unpaired, two-tailed Student's t test (PS19-T2^{CV}, $n=15$ and PS19-T2^{R47H} $n=12$).

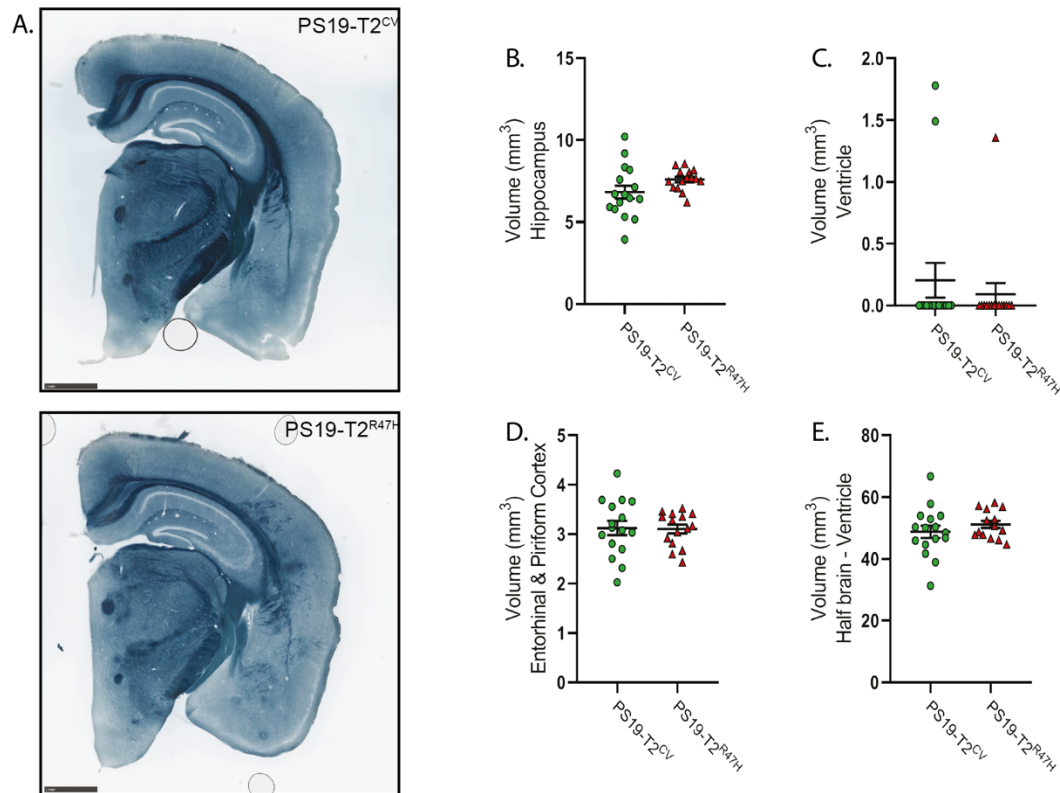


Figure S2: Impact of R47H variant of TREM2 on brain volume in 3-month-old PS19 mice. Representative images of PS19-T2^{CV} and PS19-T2^{R47H} brain sections stained with Sudan black at 3 months of age (A) (Scale bars, 1 mm). Quantification of the average volume of the hippocampus (B), ventricles (C), entorhinal and piriform cortex (D) and half brain minus ventricle (E). Data are presented as mean \pm SEM. Significance was determined by an unpaired, two-tailed Student's t test (PS19-T2^{CV}, n=16 and PS19-T2^{R47H} n=15).

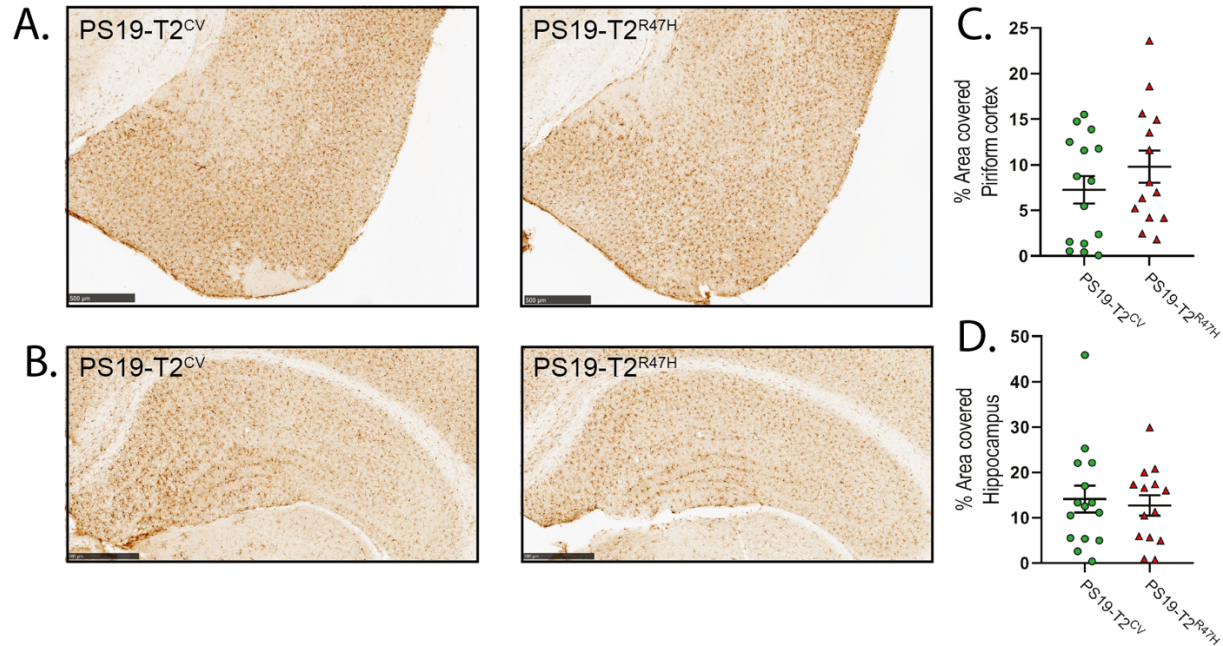


Figure S3: Impact of R47H variant of TREM2 on microgliosis in 3-month-old PS19 mice. Representative images of Iba1 staining in the piriform cortex (A) and hippocampus (B) from PS19-T2^{CV} and PS19-T2^{R47H} mice. (Scale bars: 0.5 mm). Quantification of the percent area covered by Iba1 staining in the piriform cortex (C) and hippocampus (D). Data is presented as mean \pm SEM. Significance was determined using an unpaired, two-tailed Mann Whitney's test due to the nonparametric data set (PS19-T2^{CV}, n=15 and PS19-T2^{R47H} n=14).

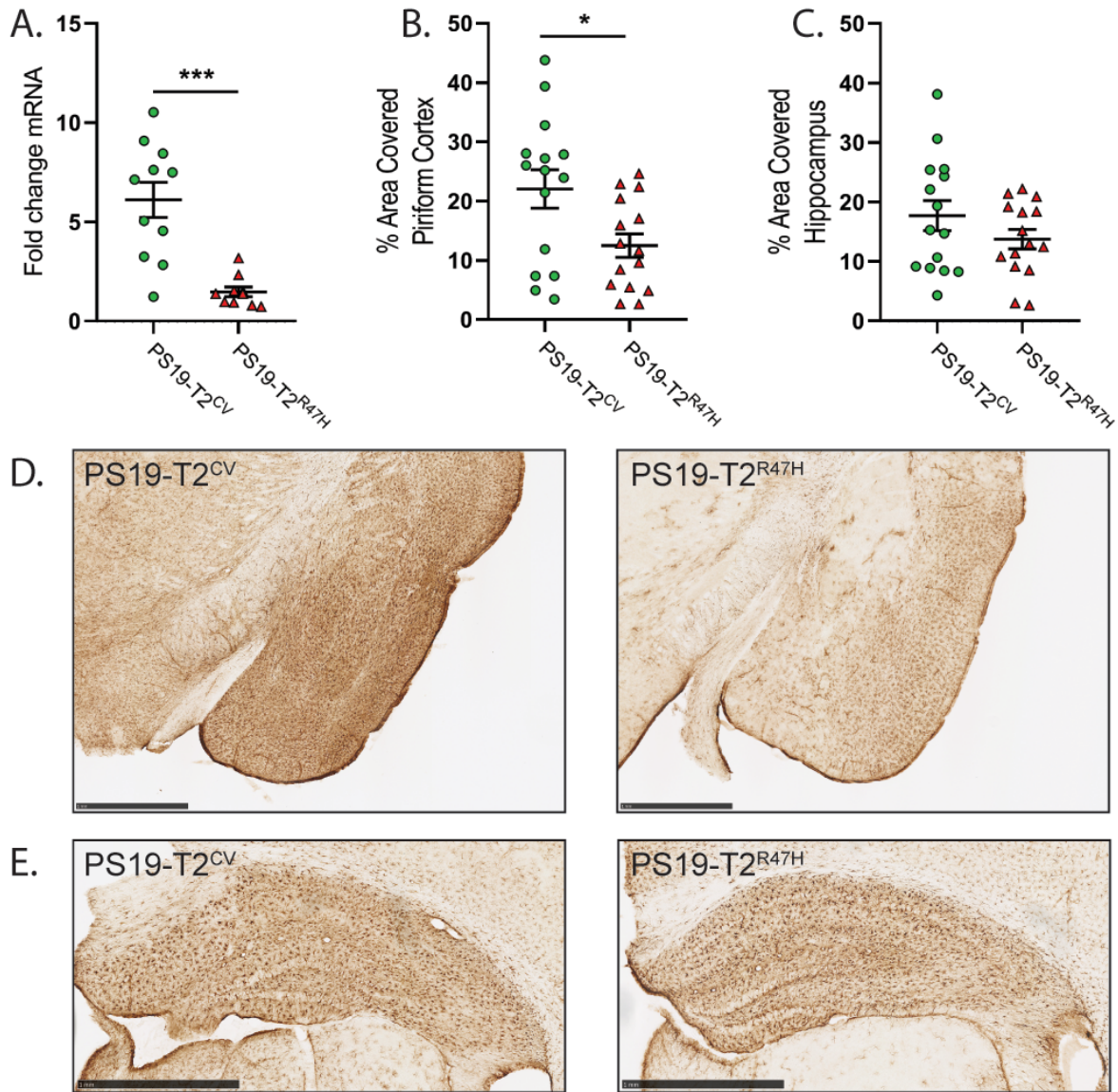


Figure S4: R47H variant of TREM2 decreases astroglialosis in 9-month-old PS19 mice. Expression of cortical GFAP mRNA of 9-month-old PS19-T2^{CV} and PS19-T2^{R47H} mice (A) (PS19-T2^{CV}, n=11 and PS19-T2^{R47H} n=10). Quantification of the percent area covered by GFAP staining in the piriform cortex (B) and hippocampus (C) (PS19-T2^{CV}, n=15 and PS19-T2^{R47H} n=15). Representative images of GFAP staining in the piriform cortex (D) and hippocampus (E) from PS19-T2^{CV} and PS19-T2^{R47H} mice (Scale bars: 1 mm). Data are presented as mean \pm SEM. Significance was determined by an unpaired, two-tailed Student's t test. Significance was defined as * p < 0.05 and *** p < 0.001

TREM2 genotype	APOE genotype	Age	Sex	CDR	Braak
CV	23	91.081	M	3	V
CV	34	81.259	F	3	VI
CV	44	72.203	M	3	VI
CV	24	88.764	F	3	VI
CV	33	90.2642	F	2	VI
CV	33	80.975	M	3	VI
CV	33	95.734	F	3	VI
CV	34	84.471	F	1	III
CV	33	91.165	M	1	III
R47H	33	90.642	M	3	V
R47H	34	88.225	F	3	IV
R47H	33	85.637	M	3	V
R47H	33	93.985	F	3	NA
R47H	34	78.231	M	3	V
R62H	34	77.714	M	3	V
R62H	34	78.981	F	3	NA
R62H	33	84.375	F	3	VI
R62H	34	89.306	F	3	VI
R62H	44	89.369	F	3	NA

Supplementary Table 1. Demographic information for TREM2^{R47H}, TREM2^{R62H}, and TREM2^{CV} AD cases used in figure 7. NA: Not Available.